

OTTO-VON-GUERICKE-UNIVERSITÄT MAGDEBURG

MASTER'S THESIS

Simulation of Brain Functional and Structural Connectivity on Empirical and Randomized Complex Networks

Supervisors:

Author:

Seyma BAYRAK

Prof. Dr. Jochen BRAUN

Dr. Philipp HÖVEL

Dr. Vesna VUKSANOVIC

*A thesis submitted in fulfilment of the requirements
for the degree of Master of Science in the*

*Department of Integrative Neuroscience,
Otto-von-Guericke-Universität Magdeburg*

at the research group

Bernstein Center for Computational Neuroscience Berlin, Nachwuchsgruppe,
Nonlinear Dynamics and Control in Neuroscience

December 2014



Declaration of Authorship

I, Seyma BAYRAK, declare that this thesis titled, 'Simulation of Brain Functional and Structural Connectivity on Empirical and Randomized Complex Networks' and the work presented in it are my own. I confirm that:

- This work was done wholly or mainly while in candidature for a research degree at this University.
- Where any part of this thesis has previously been submitted for a degree or any other qualification at this University or any other institution, this has been clearly stated.
- Where I have consulted the published work of others, this is always clearly attributed.
- Where I have quoted from the work of others, the source is always given. With the exception of such quotations, this thesis is entirely my own work.
- I have acknowledged all main sources of help.
- Where the thesis is based on work done by myself jointly with others, I have made clear exactly what was done by others and what I have contributed myself.

Signed:

Date:

“Ich brauche keine Waffe. Ich ermittle ausschließlich mit dem Gehirn.”

Helge Schneider

OTTO-VON-GUERICKE-UNIVERSITÄT MAGDEBURG

Abstract

Faculty of Medicine and Faculty of Natural Sciences

Department of Integrative Neuroscience,
Otto-von-Guericke-Universität Magdeburg

Master of Science

Simulation of Brain Functional and Structural Connectivity on Empirical and Randomized Complex Networks

by Şeyma BAYRAK

Blood oxygen level dependent (BOLD) contrast imaging is one of the widely used fMRI techniques to map the brain activity at resting-state, i.e. in the absence of any stimulus-driven task. The BOLD fluctuations arising from changing neuronal activity at resting-state have been observed to be complex but highly structured and robust [1–3]. A well-explored BOLD response of in the brain would potentially lead to easier diagnosis of neurodegenerative disorders such as Alzheimer’s disease and Parkinson’s disease. However, the underlying biophysical mechanism of the resting-state activity of the brain has not yet been completely uncovered. This master’s project combines experimental and modeling approaches in order to investigate the temporal and structural dynamics of the brain. It is aimed to *i*) demonstrate how functionally correlated behavior among cortical and subcortical brain regions emerge from the structural connectivity, *ii*) explore whether or not topological properties of brain network is distinguishable than that of its randomized networks.

The functional connectivity map derived from fMRI-BOLD measurement and anatomical connectivity map obtained from DW-MRI technique are main sources of the experimental data. Both empirical data structures are extracted by the measurements from the same cortical, sub-cortical brain regions, which are predefined by automated anatomical labeling (AAL) [4].

The modeling methods are drawn from nonlinear and network science. The temporal dynamics of the neuronal activity is simulated with FitzHugh-Nagumo (FHN) network oscillations and the BOLD activity is inferred via the Balloon-Windkessel hemodynamic model [5, 6]. The spatial dynamics of brain is analyzed by comparing brain graphs to the random networks. The brain graphs are constructed on the empirical imaging data. The random networks are generated with Erdos-Renyi-type and configuration model algorithms applied to the brain graphs.

The major results are demonstrated in three main category; comparison of *i*) simulated FHN network model time-series of brain networks to the empirical fMRI-BOLD and DW-MRI results, *ii*) simulated BOLD fluctuations of anatomical connectivity map to the fMRI-BOLD data, *iii*) the FHN network modeled neuronal activity of brain graphs to that of randomly generated networks. All comparisons are quantified with statistical methods on parameter spaces. The results indicate that, it is possible to explore such regions in the parameter spaces, where *i*) BOLD fluctuations are captured through structural brain connections, *ii*) network measures as well as temporal dynamics of brain graphs are different from that of random graphs.

This project provides a deeper insight to the coupled relation between functional and anatomical brain connectivity: how the non-random dynamical process of brain's functional connectivity could be shaped by its structural topology.

Acknowledgements

I would like to thank my supervisors, Dr. Philipp Hövel and Dr. Vesna Vuksanović, for their valuable guidance, productive criticism and highly communicative working environment throughout my Master's project. I would especially like to express gratitude to my supervisors for their prompt and highly responsive feedback while I conducted my Master's research. It was a great experience to participate in scientific seminars and conferences related to the field of my research that gave me the unique opportunity to exchange ideas with pioneers in the field of computational neuroscience. I would also like to thank Prof. Jochen Braun for his advice on my project, my future academic career and for organizing the defense committee in Magdeburg. I am particularly grateful to my boyfriend, Rüdiger Meier, who has supported me during the writing of my thesis with his amazing computational skills, delicious home-baked cookies and most importantly, constant encouragement. I would like to thank Prof. Benjamin Lindner and all the people in his research group for the discussions on my thesis and for enjoyable table-soccer sessions after lunch. I am thankful to Yasser Iturria-Medina for sharing the DW-MRI data used in this project. This Master's thesis is embedded in the Bernstein Center of Computational Neuroscience Berlin and it is supported by DAAD-TEV (German Academic Exchange Service - Turkish Education Foundation) as part of its Master's program scholarships for Turkish students in Germany.

Contents

Declaration of Authorship	i
Abstract	iii
Acknowledgements	v
Contents	vi
List of Figures	viii
List of Tables	x
Abbreviations	xi
Symbols	xii
1 Introduction	1
2 Methods and Models	5
2.1 Empirical Brain Connectivity Maps	6
2.2 The Brain Graph	8
2.3 Randomization Methods	10
2.3.1 Erdős-Rényi-Type Randomization	10
2.3.2 Double-Edge-Swap Type Randomization	11
2.3.3 Preserved-Degree-Distribution Type Randomization	12
2.3.4 Configuration Model Randomization	13
2.3.5 Partial Randomization	14
2.4 Network Characterizations	16
2.4.1 Network Density	16
2.4.2 Average Clustering Coefficient	17
2.4.3 Transitivity	18
2.5 FitzHugh-Nagumo Model for Neuronal Activity Simulation	20
2.5.1 FitzHugh-Nagumo Model Local Dynamics	21
2.5.2 Noise Effect	24
2.5.3 Coupled Dynamics	24
2.5.4 Network Dynamics	26
2.6 Balloon-Windkessel Model for BOLD Activity Simulation	28

2.6.1	Hemodynamic Model	30
3	Results	33
3.1	Neuronal Activity Simulations	34
3.1.1	Functional Brain Graphs Compared to fMRI-BOLD Data	34
3.1.2	Anatomical Brain Graphs Compared to DW-MRI Data	38
3.2	BOLD Activity Simulations	42
3.3	Comparison of Brain Graphs to Random Graphs	47
3.3.1	Comparing Functional Brain Graph to the Random Graphs	49
3.3.2	Comparing Anatomical Brain Graph to the Random Graphs	52
4	Conclusion and Discussion	56
A	Automated Anatomical Labeling	59
B	Network Characterizations	61
B.1	Average Degree	61
B.2	Average Shortest Pathway	62
B.3	Global Efficiency	63
B.4	Local Efficiency	63
B.5	Small Worldness	64
B.6	Assortativity	65
B.7	Average Connected Components	66
B.8	Degree Distribution	67
B.9	Clustering Coefficient of Nodes	70
C	Empirical Distance Matrices	72
Bibliography		73

List of Figures

2.1	Empirical FCM and ACM	8
2.2	Empirical FCM and ACM in Cortex	8
2.3	Binarizing via Thresholding	10
2.4	Erdos-Renyi Example	11
2.5	Double-Edge-Swap Example	12
2.6	Degree Distribution 2D Example	13
2.7	Degree Distribution 3D Example	13
2.8	Degree Sequence Definition	14
2.9	Partial Randomization Example	15
2.10	Network Density	17
2.11	Clustering Coefficient	18
2.12	Transitivity	19
2.13	FHN Local	23
2.14	FHN Noise	24
2.15	FHN Global	25
2.16	FHN Graph	27
2.17	FHN Time Series	27
2.18	Hemodynamic Model	30
3.1	Neural Activity Node Dynamics, FCM	35
3.2	High Correlated FHN Simulation, FCM	36
3.3	Parameter Analysis, FCM	37
3.4	3D Fast Fourier Transform, FHN, FCM	37
3.5	Parameter Analysis, ACM	39
3.6	High Correlated FHN Simulation, ACM	39
3.7	Neural Activity Node Dynamics, ACM	40
3.8	3D Fast Fourier Transform, FHN, ACM	41
3.9	Parameter Analysis, BOLD	43
3.10	High Correlated BOLD Simulation, FCM	44
3.11	BOLD Activity Node Dynamics, FCM	44
3.12	High Correlated BOLD Simulation, ACM	45
3.13	BOLD Activity Node Dynamics, ACM	46
3.14	3D Fast Fourier Transform, BOLD, FCM	47
3.15	Sample Histogram for Brain Graph	48
3.16	Histogram Comparison, FCM	50
3.17	Random Graph Comparison, FCM	51
3.18	Histogram Comparison, ACM	53
3.19	Random Graph Comparison, ACM	54

B.1	Average Degree	61
B.2	Shortest Pathway	62
B.3	Global Efficiency	63
B.4	Local Efficiency	64
B.5	Small Worldness	65
B.6	Assortativity	66
B.7	Average Connected Components	67
B.8	Degree Distribution, FCM	68
B.9	Degree Distribution, ACM	69
B.10	Clustering Coefficient of Nodes, FCM	70
B.11	Clustering Coefficient of Nodes, ACM	71
C.1	Distance Matrices	72

List of Tables

2.1 Abbreviations of Randomization Methods	15
2.2 BOLD Model Parameters	30
A.1 Automated Anatomical Labeling for the Brain Regions	60

Abbreviations

AAL	Automated Anatomical Labeling
AC	Anatomical Connectivity
ACM	Anatomical Correlation Matrix
AM	Adjacency Matrix
BOLD	Blood Oxygen Level Dependent
CBF	Cerebral Blood Flow
CBV	Cerebral Blood Volume
CM	Correlation Matrix
CMRO₂	Cerebral Metabolic Rate (of) O ₂ (consumption)
dHb	deoxygenated Hemoglobin
DW-MRI	Diffusion Weighted Magnetic Resonance Imaging
FC	Functional Connectivity
FCM	Functional Correlation Matrix
FFT	Fast Fourier Transform
fMRI	functional Magnetic Resonance Imaging
FHN	FitzHugh-Nagumo
Hb	(oxygenated) Hemoglobin

Symbols

r	threshold	
p	probability	
N	total number of nodes	
L	total number of edges	
k_i	degree of node i	
$\langle k \rangle$	average degree	
$p(k)$	degree distribution	
$P(k)$	cumulative degree distribution	
κ	network density	
C_i	clustering coefficient of node i	
C	average clustering coefficient	
t_i	number of triangles around node i	
T	transitivity	
E	global efficiency	
E_{loc}	local efficiency	
S	small worldness	
A	assortativity	
a_{ij}	adjacency matrix element	$a_{ij} \in \{0, 1\}$ where $i, j = 1, \dots, N$
d_{ij}	distance matrix element	$i, j = 1, \dots, N$
ρ	Pearson correlation coefficient	
$d(A, B)$	Bhattacharya coefficient	A, B are histograms
\mathbf{J}	Jacobian matrix	
λ	eigenvalue	
c	coupling strength	
v	axonal signal propagation velocity	$[v] = \text{m/s}$

Δt_{ij}	time delay between nodes i and j
τ	time constant of FHN model
D	strength of Gaussian white noise
I	external stimulus
ν	frequency [ν] =Hz
s	blood flow inducing signal
τ_s	time constant of s
f_{in}	CBF (inflow)
τ_f	feedback time constant
V	CBV
τ_0	mean transit time of V
f_{out}	CBF (outflow)
E_0	resting net O_2 extraction rate
q	dHB content in voxel

Chapter 1

Introduction

The purpose of this master's project is to quantify large-scale functional and structural brain networks and the comparison to resting-state functional Magnetic Resonance Imaging (fMRI). The functional brain networks are derived from simulated blood oxygen level dependent (BOLD) signals, whereas the structural brain networks are obtained from diffusion weighted magnetic resonance imaging (DW-MRI). The project uses experimental results combined with modeling approaches and implements methods drawn from nonlinear and network science.

Large-scale functional brain connectivity maps are networks of brain regions based on functional interactions, i.e. any co-activation between these regions [1–3]. In a typical fMRI experiment, functional connections are obtained from pre-defined brain regions, whose corresponding time-series of BOLD activity display significant correlations at low-frequencies (< 0.1 Hz). Measured BOLD activity patterns are complex, but they are also highly structured and robust. Moreover, structural motives of the correlated activity have been reported not only during brain's activation paradigm, but also in the course of so-called resting state, i.e. under no stimulation and in the absence of any stimulus-driven task. Despite its importance, the underlying biophysical process of the resting activity of the brain has not yet been fully resolved. One of the main objectives in this project is to capture resting state BOLD fluctuations by modeling time-series and BOLD activity for nerve cell populations in the brain.

DW-MRI technique estimates the structural connection probabilities among brain regions indirectly by investigating the diffusion direction of water molecules. The direction

of the fiber tracks in white matter depends indirectly on the diffusion of water molecules. A DW-MRI experiment approximates the existence of a fiber track between regions of interest. Both anatomical and functional brain connectivity maps used in this project are empirically obtained from the same cortical and sub-cortical regions. For this purpose, the brain images are partitioned into $N = 90$ regions based on the Tzourio-Mazoyer brain atlas using the automated anatomical labeling (AAL) method [4]. In fact, it will be discussed how functional connections between brain regions could arise from complex structural connections.

Despite important progress over the past few years, the way how functional connectivity arises from the complex anatomical connectivity still remains poorly understood [7]. Existing models of resting-brain dynamics hypothesize that functional interactions result from a complex interplay between intrinsic brain dynamics and underlying structural connections [8]. In particular, these models explore the range of conditions at which functional networks emerge from anatomical connections, the role of multiple time-scales in the formation of functional connectivity networks [9], time delays in the signal propagation between the network nodes as well as the system noise [10, 11], local network oscillations [12, 13] and structural disconnection [14].

The neuronal activity model of the resting activity of brain is built on FitzHugh-Nagumo (FHN) oscillators as previously proposed in [5, 7]. The temporal dynamics of membranous potential of each AAL region (a single *node*) is simulated with FHN model. The model parameters are tuned in such a way that the dynamics of nerve cells in each node exhibit type-II excitability. One of the key ingredients of the network model is the *coupling strength* c , which scales mutual time-delayed functional interactions among brain regions globally. The time-delay in the model appears as a natural consequence of a finite speed of signal propagation along axons. Therefore, the *signal velocity* v , representing biophysically realistic axonal signal propagation [10–12] is considered to be another significant ingredient for FHN dynamics.

FHN model is used to extract time-series for AAL regions based on functional and anatomical brain networks. However, high frequency FHN oscillations need to be tuned into slow fluctuations in order to capture BOLD signals observed in fMRI. The BOLD activity is inferred via the Balloon-Windkessel hemodynamic model, which takes the simulated neuronal activity time-series as an input and gives the simulated BOLD activity

as an output [6]. In this project, the hemodynamic model is applied on FHN time-series extracted from functional and anatomical brain networks. Then, any correlation matrix based on simulated BOLD signal is statistically compared to the empirical correlation matrix based on fMRI-BOLD.

Functional and anatomical brain networks are constructed after binarizing via thresholding the fMRI-BOLD and DW-MRI data, respectively. The spatial dynamics of each network is identified in dependence on the threshold level; r for functional connectivity (FC) and p for anatomical connectivity (AM). Statistical characterization of brain networks, using methods from graph theory, has revealed some of their key topological properties such as small worldness, modularity or resilience to attacks, that is node or link removal [15]. This project studies these properties both for functional and structural brain networks, which arise from modeled intrinsic brain dynamics. In particular, I aim to explore such conditions that distinguish obtained network topologies from that of random networks. Several randomization procedures are considered. They include, but are not limited to random networks of Erdős-Rényi-type with the same number of nodes and links as in the empirically derived case. This approach is expected to provide a deeper insight into the underlying processes involved in the observed functional connectivity and their relations to the coupling topology, i.e., brain structural connectivity.

The rest of the master's thesis is organized in the following order: Empirical data sets of FC and AC matrices are introduced in Section 2.1, and it is further extended with brain graph construction based on these connectivity maps in Section 2.2. Section 2.3 explains the randomization methods used to build random graphs. Characterization of all constructed networks by using methods of network science [8, 16–18] is done by quantifying global and local network properties such as network density, clustering coefficient and small-worldness in Section 2.4. Temporal dynamics emerging from the FitzHugh-Nagumo model and the Balloon-Windkessel hemodynamic model [6] are described in Sections 2.5 and 2.6. Section 3.1 illustrates simulated neuronal activity results, i.e. the statistical comparison of FHN simulated brain graphs to the fMRI-BOLD data in parameter space of (r, c) and (r, v) . Section 3.2 demonstrates simulated BOLD fluctuations applied on functional and anatomical brain graphs. Section 3.3 compares the modeled temporal dynamics of brain graphs to that of random networks with a statistical quantification. Finally, Section 4 concludes the master thesis with the research proposals: it is possible to explore such regions on parameter space, where $i)$ BOLD fluctuations

are captured through structural brain connections *ii)* network measures and temporal dynamics of brain graphs are different from that of random graphs.

Chapter 2

Methods and Models

In this section, the construction of brain graphs based on empirical functional connectivity matrix (FCM) and anatomical connectivity matrix (ACM) will be first introduced. Then, the topological characteristics of all graphs will be statistically measured and those topological measures will be interpreted neuro-biologically. In particular, it is aimed to explore under which conditions that brain network topologies distinguish from random networks. For this purpose, tools and concepts from graph theory / network science will be used. This approach is expected to provide a deeper insight into the underlying process involved in the observed functional and structural brain connectivity.

Graph theory is a mathematical field applicable to a large diversity of complex systems such as markets, ecosystems, computer circuits, and gene-gene interactions [19]. A graph is defined as an ensemble of vertices (nodes) that are connected by edges (links). If the edges connect the nodes in a specified direction, the graph is referred to as *directed*, otherwise *undirected*. Moreover, the edges can be assigned a weight yielding a *weighted* graph. A graph with edges of uniform weight is called an *unweighted* graph.

Network science incorporates graph theory applied on a distinct complex domain. Unlike classical graph theory, network science primarily deals with real-life networks that are large and complex - neither uniformly random nor ordered [20]. The neuro-anatomical and neuro-physiological data sets derived from DW-MRI and fMRI-BOLD techniques can be considered as such large-scale complex brain graphs, that can be modeled as *undirected* and *unweighted* networks for simplicity. Nodes in large-scale brain networks

usually represent brain regions, while edges represent anatomical, functional or effective connections [21].

A brain network can be statistically described in terms of its topology, i.e. solely in terms of its connectivity and independently of spatial positions of nodes and edges. Topological measures described in previous studies capture local and global properties of a network, e.g. local and global efficiency, clustering coefficient, transitivity and small-worldness [22–25].

Methods of graph theory applied to structural and functional systems have shown that both share typical features of many complex networks [7, 8, 15, 26]. However, the essential features of brain’s connectivity still remain ambiguous both for functional and structural maps. This project aims to investigate whether or not the brain behaves as a completely random circuitry. This idea will be tested by comparing brain graphs to the randomized networks as it was previously noticed by Bullmore and Bassett [27]. The majority of random graphs here are inspired by Erdős-Rényi-type random networks and the configuration model.

The following subsections will introduce building real-networks given empirical brain connectivity maps, generating random networks by manipulating the brain graphs with randomization procedures and quantifying the spatial characteristics of all graphs constructed. Once the graph theory related methods are covered, the temporal dynamics for the neuronal activity and BOLD fluctuations will be explained in further subsections of Chapter 2.

2.1 Empirical Brain Connectivity Maps

The functional-magnetic-resonance-imaging (fMRI) is a widely used method to detect the blood oxygen level dependent (BOLD) contrast in the brain. The fMRI-BOLD contrast is used to interpret the neuronal activity in the respective voxel, which can be considered as a rectangular volume in brain defined for the imaging studies. The ongoing firing activity of neurons requires energy and it is supplied by neighboring blood cells via oxygen and glucose release into the nerve cells. The deviations in deoxygenation level, cerebral flow and volume in blood vessels due to neuronal activity, known as *hemodynamic process*, cause a change in the detected fMRI-BOLD signal strength. The

functional connectivity matrix (FCM) represents correlation coefficients of these fMRI-BOLD signals detected from the pre-defined brain regions with voxels.

The resting state empirical FCM used in this project is obtained from the *1000 Functional Connectome Project* website (<http://www.nitric.org/>). The human brain is segmented into $N = 90$ cortical and sub-cortical regions according to the Tzourio-Mazoyer brain atlas with the automated anatomical labeling (AAL) template [4], such that regions with index $n = \{1, 2, \dots, 45\}$ lie on the right hemisphere, whereas $n = \{46, 47, \dots, 90\}$ are on the left (Appendix A). The fMRI-BOLD activity is measured from all voxels in an AAL region for 7.5 min of acquisition time. Once the fMRI-BOLD mean time-series are obtained for all AAL regions, the FCM is obtained by calculating the Pearson correlation coefficients of time-series between all pairs of the 90 AAL regions. Therefore the size of FCM is $N \times N = 90 \times 90$. To be more precise, BOLD-fMRI signal is averaged for the same subject over voxels in an AAL region, and FCM is averaged over all subjects at the end.

The diffusion weighted magnetic resonance imaging (DW-MRI) technique estimates the anatomical connection probabilities among brain regions by investigating the diffusion direction of water molecules within a voxel. The direction of the fiber tracks in white matter depends on the diffusion pattern of water molecules. A DW-MRI experiment approximates the existence of a fiber track between regions of interest. The anatomical connectivity matrix (ACM) used in this project is obtained from the study of Iturria-Medina et al. [28] and it is based on the same $N = 90$ AAL regions as in the FCM described above. The size of ACM is also $N \times N = 90 \times 90$, and each value reveals the probability of 2 AAL regions being connected via axonal fibers.

Figure 2.1 represents empirically captured FCM and ACM. All correlation coefficients in FCM appear in the range $[0,1]$ as well as all probability values in ACM. Both matrices are symmetric. A correlation value close to 1 in FCM indicates that the quantified functional activities of corresponding nodes in the right and left hemisphere highly resemble each other (see sub-diagonals in Figure 2.1, left). A probability value close to 1 in ACM demonstrates that corresponding nodes are most likely connected by fiber tracks in white matter. Although some node pairs are not anatomically coupled at all in ACM (cold colors), they could be functionally coupled in FCM (hot colors). This is especially true for the corresponding regions in the different hemispheres.

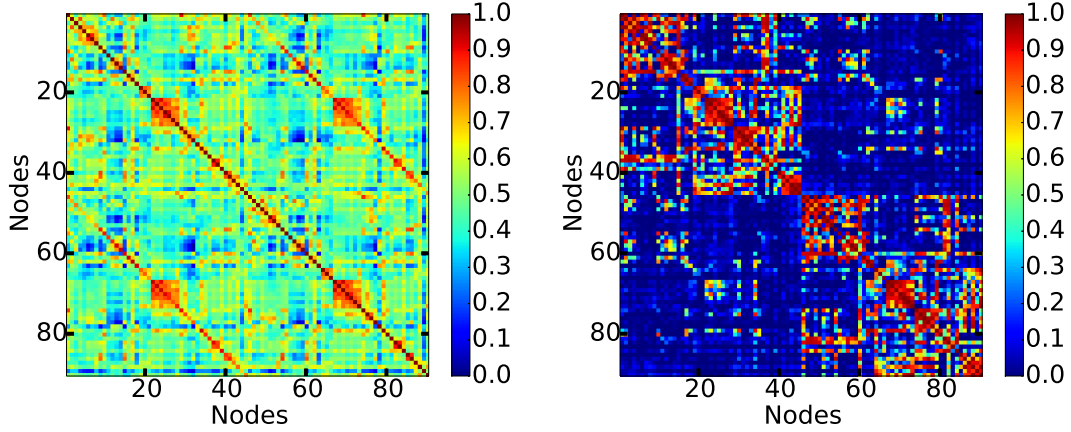


FIGURE 2.1: Empirical functional and anatomical connectivity maps of human cortex, FCM obtained from fMRI-BOLD technique (on the left) and ACM obtained from DW-MRI (on the right). The colorbars exhibit correlation coefficients and probability values in FCM and ACM, respectively.

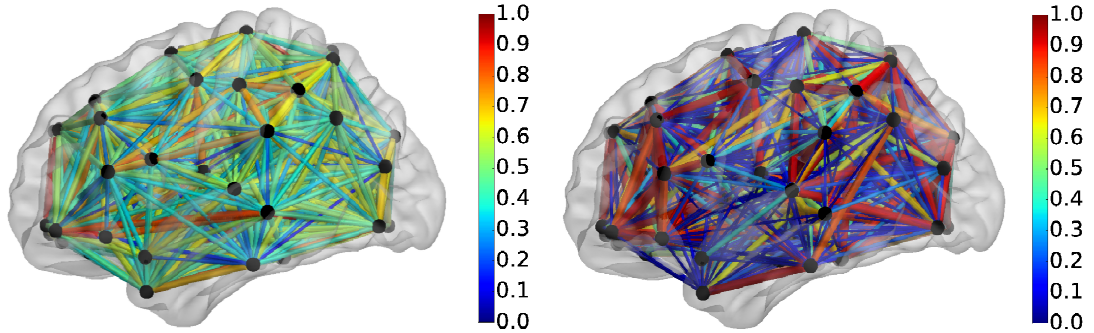


FIGURE 2.2: 3D sagittal visualization of empirical FCM (on the left) and ACM (on the right) on the human cortex with the BRAINNET VIEWER. The colorbars are the same as explained in Figure 2.1. [29].

FCM and ACM are embedded in human cortex in Figure 2.2 [29]. All nodes are presented with equal size and black color independent of their topological properties. However, edges have different thickness and color distribution according to correlation coefficients and probability values with respect to FCM and ACM.

2.2 The Brain Graph

The brain graphs considered here are derived from two sets of empirical brain connectivity maps: FCM and ACM obtained from fMRI-BOLD and DW-MRI techniques, respectively. Those data sets represent measurements from $N = 90$ cortical and subcortical regions labeled with AAL, represented by nodes in the graph. The nodes can

be connected to each other by means of *edges*. If the graph is constructed on the FCM, edges are interpreted as correlation strengths between the functional BOLD activity of two nodes. If the graph is built on the ACM, an existing edge is considered as the probability of two nodes to be structurally connected by fiber tracks in white matter.

The brain graphs in this project are generated through binarizing the functional connectivity matrix (FCM) and anatomical connectivity matrix (ACM). Binarization here means converting all the values in a given matrix into 1's and 0's via thresholding. Because of the nature of their definition, both empirical data sets have values between 0 and 1, reflecting a correlation strength in case of FCM or a probability value in case of ACM. We arbitrarily define a threshold value r for the strength of correlations in FCM. Then, the values greater and equal to r are assigned the value 1, while others are set to 0. This thresholding is applied by means of the strength of probability value, p , for the ACM. The binarized matrix is the basis of brain graph construction, and it is commonly known as *adjacency matrix*. The NETWORKX software package in PYTHON is used to build graphs given adjacency matrices [30]. Neither the direction of functional or anatomical connectivity between nodes, nor any other values apart from 0 and 1 are encoded in the adjacency matrices so that the resulting graphs are considered as *undirected* and *unweighted*. In other words, all existing edges are thought to be of uniform weight and nodes interact both ways along an edge connecting them.

Figure 2.3 illustrates the exemplary construction of a brain graph from the FCM. All correlation values among the cortical and sub-cortical regions in the empirical fMRI-BOLD data lie between 0 and 1. The 3D axial cortex visualization represents only the existing edges with black edges among the nodes. The adjacency matrix (AM) is filled out only with 1's and 0's indicating functionally connected and unconnected nodes, whose correlated BOLD activity is equal to or greater than $r = 0.55$. The algorithm NETWORKX builds the corresponding brain graph of an adjacency matrix [30]. The AM obtained from an ACM would look similar, but would represent the probability of two nodes to be anatomically connected above a predefined threshold p .

The following sections will cover randomization methods reshuffling the brain graphs and introduce some of the topological concepts characterizing brain graphs as well as random networks.

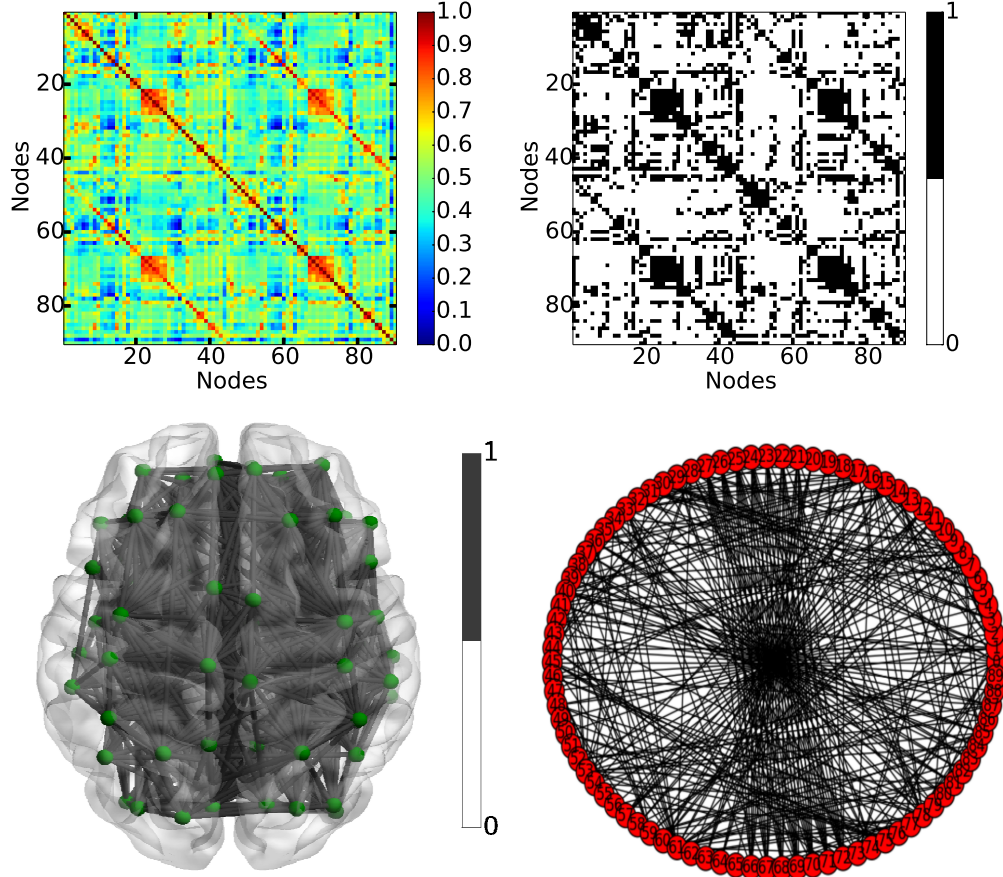


FIGURE 2.3: How to build a brain graph: The empirical data matrix derived from fMRI-BOLD technique (upper left) is binarized via a threshold value $r = 0.55$ and its corresponding adjacency matrix (upper right). The black spots represent 1's indicating edges between nodes, whereas the white squares represent 0's implying no edge. The adjacency matrix is embedded on human cortex axially (lower left) with BRAINNET VIEWER [29] and the brain graph derived from the adjacency matrix with NETWORKX [30] (lower right).

2.3 Randomization Methods

2.3.1 Erdős-Rényi-Type Randomization

Given a total number of nodes N , Paul Erdős and Alfréd Rényi produced an undirected graph $G(N, P)$, in which the presence of any edge between two nodes is assigned a probability P . The average total number of edges L in an Erdős-Rényi-type random graph is $\binom{N}{2}P$, with a binomial distribution for the number of edges per node, known as the *degree* of a node [31].

New randomization techniques arise through modifying the Erdős-Rényi method, e.g. given N and L , a graph $G(N, L)$ can be picked uniformly random out of the set of all

potential graphs having N nodes and L edges, which means the same network *density*. The probability for a graph to be picked among all the others is $\frac{L}{\binom{N}{2}}$. One can study the various aspects of $G(N, P)$ and $G(N, L)$ even more detailed, but for the sake of simplicity, Erdős-Rényi model will not be discussed further here [17, 31].

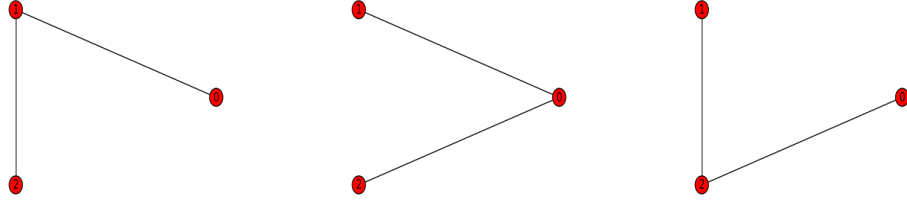


FIGURE 2.4: An illustration of the set of all $G(N, L)$ type random graphs with $N = 3$ and $L = 2$.

Figure 2.4 illustrates all possible graphs having 3 nodes and 2 edges. One of those 3 simple graph is chosen uniformly random for the $G(N, L)$ randomization type, so that each graph is chosen with probability $P = \frac{1}{3}$.

The $G(N, L)$ type randomization is the first method used to derive random graphs from the adjacency matrices of FCM and ACM in this project. Both matrices have $N = 90$ nodes. However L changes for each brain graph according to the applied threshold level and therefore is always recalculated.

2.3.2 Double-Edge-Swap Type Randomization

The *degree* k_i of a node i is defined as the number of edges connected to that node. The double-edge-swap method manipulates a given graph by swapping two existing edges among four nodes, while keeping the node degrees fixed.

Figure 2.5 illustrates randomly chosen double edges in a sample graph to be swapped. After the existing edges are removed, the new pair of nodes are rewired. The degree of each node is the same before and after swapping; degrees of nodes $k_1 = 1$, $k_2 = 1$, $k_3 = 1$, $k_4 = 1$ are all fixed in each graph. Although the randomly constructed graphs with the double-edge-swap method are expected to have same degrees, the latter is not a unique property identifying a graph.

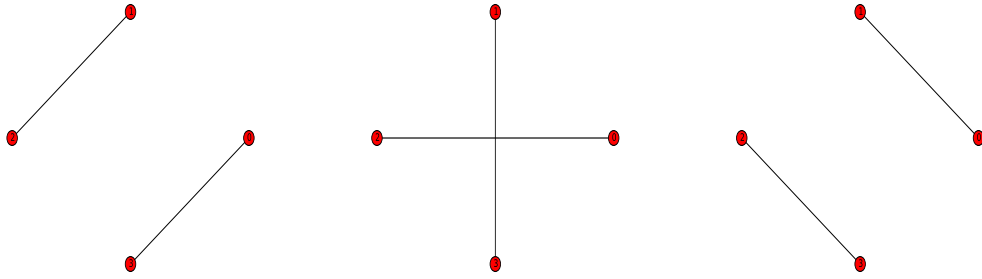


FIGURE 2.5: Swapping edges between 2 paired nodes.

The *degree distribution* is the probability distribution of node degrees over the whole graph. Conservation of each k_i preserves the degree distribution, however, preserving degree distribution does not guarantee to fix k_i values. We will discover in the next section how to preserve degree distribution by altering node degrees.

2.3.3 Preserved-Degree-Distribution Type Randomization

The preserved-degree-distribution method randomizes a given network by rewiring its edges while recovering its degree distribution $p(k)$. The sum of degree distributions and cumulative distribution $P(k')$ can be stated algebraically with the following equation,

$$1 = \sum p(k), \quad P(k') = \sum_{k \geq k'} p(k), \quad (2.1)$$

where $p(k)$ is the probability of a node to have degree number k [32].

The algorithm for the preserved-degree-distribution is adapted from *Brain Connectivity Toolbox* (BCT) [33]. Figure 2.6 demonstrates a sample graph and its randomized version via preserved-degree-distribution method. Not only the $p(k)$, but also the individual node degrees k_i do not go under any change. The algorithm resembles highly the double-edge-swap type randomization tool implemented from NETWORKX [30]. However, it ensures that the graph stays *connected*, i.e. it is always possible to reach a node through any other node in the graph.

$p(k)$ is a global topological measure for a network, it can be illustrated over all nodes in the whole graph as in Figure 2.7. Node indices are labeled on x -axis of the heat map,

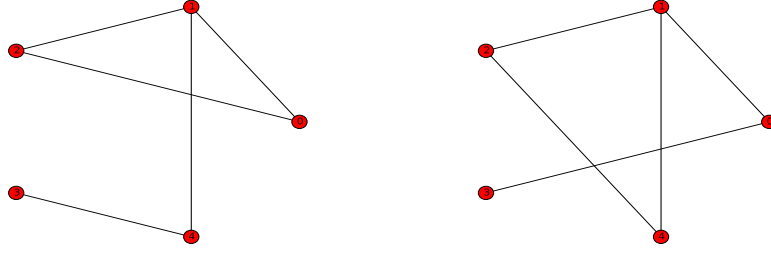


FIGURE 2.6: A sample graph (left) and its randomized version (right) with preserved-degree-distribution method. $p(k=1) = \frac{1}{5}$, $p(k=2) = \frac{3}{5}$, and $p(k=3) = \frac{1}{5}$ in both graphs.

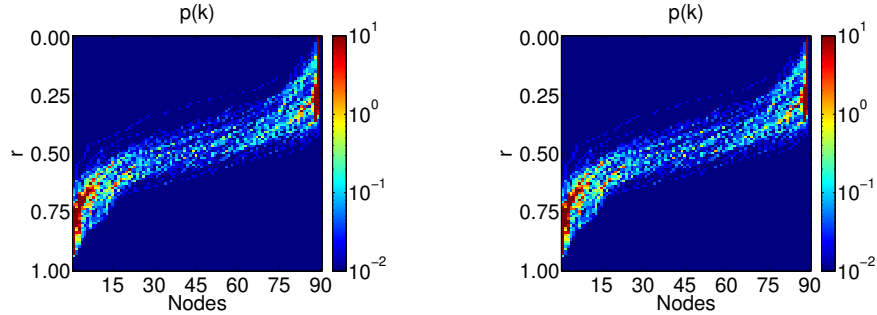


FIGURE 2.7: Heat maps for degree distributions of the brain graph (obtained from functional connectivity map of brain, fMRI-BOLD data) (left), and of the randomized graph with preserved-degree-distribution tool (right). Colorbars are in logarithmic scale.

threshold r values for adjacency matrices are given on y -axis. The preserved-degree-distribution method generates successfully a random graph with the same $p(k)$ as in the brain graph.

2.3.4 Configuration Model Randomization

The *degree sequence* of a graph is either its ascending or descending sequence of node degrees. The configuration model generates a random graph with a given degree sequence. The direct implementation of this model is to assign edges to the nodes randomly until the desired degree sequence is matched. The resulting random graph is expected to be

a node-index-shuffled version of the original graph. However, these algorithms are non-trivial due to the occurrence of self-loops (node is connected to itself) and parallel edges (multiple edges connecting two nodes), which are both undesirable graph properties in this project.

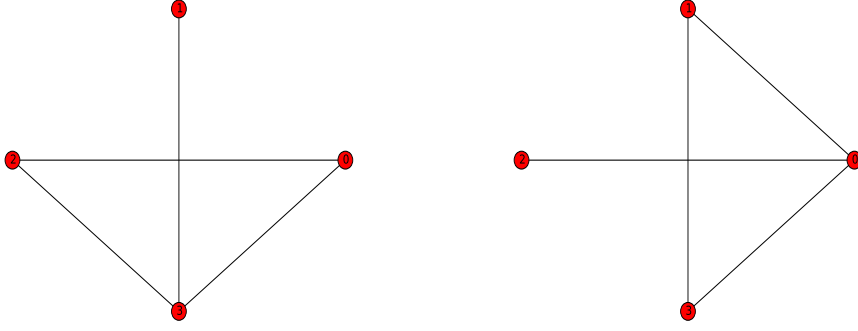


FIGURE 2.8: The degrees of the nodes in the original graph (left): $k_0 = 2$, $k_1 = 1$, $k_2 = 2$, $k_3 = 3$ and that of the randomized graph (right): $k_0 = 3$, $k_1 = 2$, $k_2 = 1$, $k_3 = 2$. The degree sequence in non-increasing order in both graphs: $\{3, 2, 2, 1\}$

Figure 2.8 points out the relevance of the degree sequence to the node degrees. Moreover, one should not confuse degree distribution and degree sequence.

The configuration model variant used here is the expected-degree-graph method, which excludes self-loops and parallel edges. This algorithm receives the list of the expected degree sequence as an input $(k_u, k_v, k_m, k_l, \dots)$, and assigns edges between nodes with a predefined probability $P_{uv} = \frac{k_u k_w}{\sum_i k_i}$. This method does not guarantee to construct graphs with exactly the same given degree sequence but with the closest possible sequence.

2.3.5 Partial Randomization

The partial randomization method reconstructs a graph (say A) with partial rewirings with respect to a second graph (say B) while keeping the degree distribution the same as in A. The analogy of this algorithm is to perform rewirings in the adjacency matrix of A, while avoiding any edge generation which already exist in the B. In other words, the choice of edges to be performed rewirings in A is limited with respect to the B.

In this project, the functional connectivity (FC) adjacency matrix is partially rewired with respect to the anatomical connectivity (AC) adjacency matrix. This means doing such rewirings among the nodes in FCM only if these nodes are not structurally connected in the brain with probability above a given value. The same procedure is done to randomize AC adjacency matrix partially with respect to FC adjacency matrix. This time nodes in ACM can be linked only if they are not functionally correlated above a given threshold.

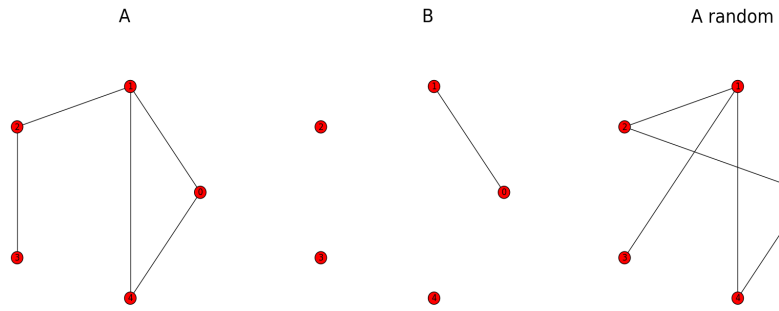


FIGURE 2.9: Graph A is performed a partial randomization with respect to graph B. While the partial randomization tool rewrites edges in A, it avoids creating such edges that exist in B.

Representative graphs *A* and *B* in Figure 2.9 can be thought as FCM and ACM, respectively. In this case, *A random* is the partially randomized graph of FCM with respect to ACM.

The brain graph and randomly generated graphs will be identified in terms of their topological properties in the following sections. For simplicity the abbreviations are introduced in the table below.

TABLE 2.1: Abbreviations for the brain graph and the randomly constructed graphs.

Abbreviation	Description	method
R_{BG}	the brain graph	NETWORKX [30]
R_{ER}	Erdős-Rényi, $G(N,L)$	NETWORKX [30]
R_{DES}	double-edge-swap	NETWORKX[30]
R_{PDD}	preserved-degree-distribution	BCT [33]
R_{CM}	configuration model	NETWORKX [30]
R_{PR}	partial randomization	BCT [33]

Section 2.1 introduced the empirical data sets used in this project; the functional connectivity (FM) map and anatomical connectivity (AM) map, which are obtained from fMRI-BOLD and DW-MRI measurements at resting state of brain. Section 2.2 brought up the construction of brain graphs based on FC and AM maps. Section 2.3 explained the randomization tools to manipulate these brain graphs topologically. The next section aims to characterize the network measures of R_{BG} and all other random graphs.

2.4 Network Characterizations

A network can be statistically described in terms of its topology, i.e. solely in terms of its connectivity and independently of spatial positions of nodes and edges. Topological measures described in previous studies capture local and global properties of a network, e.g. local and global efficiency, clustering coefficient, transitivity and small-worldness [22–25]. This section aims to characterize the topology of brain graphs obtained from FC and AC maps together with the topology of the random networks, which are generated by applying the randomization procedures on the brain graphs (Section 2.3).

2.4.1 Network Density

The *average degree* $\langle k \rangle$ of a network is proportional to the ratio of total number of edges L to total number of nodes N in a graph,

$$\langle k \rangle = \frac{2L}{N}. \quad (2.2)$$

It should be noted that in order to not count each edge twice, the total number of edges is divided by $N/2$ instead of N . The *density* κ of a network is a scaled version of average degree measurement. It is formulated as the ratio between L and maximum number of possible edges $\binom{N}{2}$,

$$\kappa = \frac{2L}{N(N - 1)}. \quad (2.3)$$

The measure of network density can be referred to as the total *wiring cost* of the network [20]. The degree, average degree and network density are key scalar measures to

characterize the topology of a network. There is, for instance, clinical evidence that reductions in nodal degree are associated with greater severity of local amyloid deposition in patients with Alzheimer's disease [34].

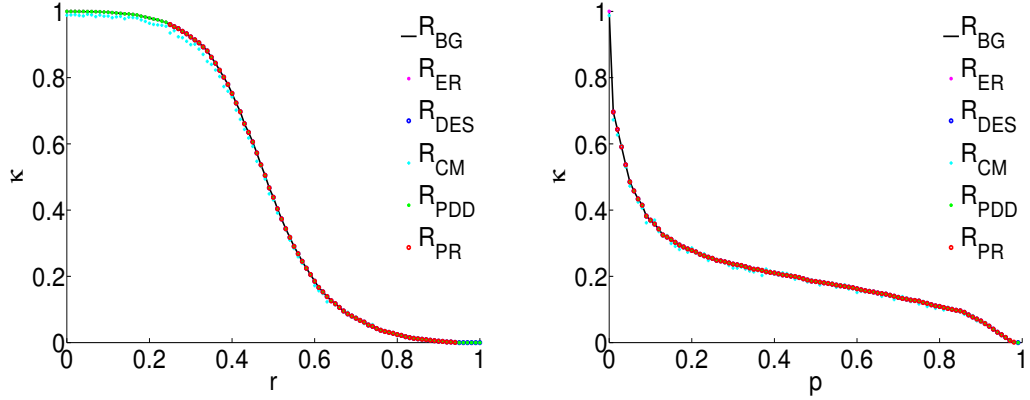


FIGURE 2.10: Network density of the brain graphs constructed on FC (left) and AM (right) maps, and their randomized networks. The abbreviations are chosen as described in Table 2.1.

The network density κ can be considered a probability for all graphs in corresponding threshold r and p ranges. The random networks are built in such ways that they have the same number of nodes and almost the same κ as in the brain graphs. However, the κ is not a unique metric identifying a network.

Figure 2.10 shows that all networks are densely connected for low r and p . For the functional R_{BG} and its randomized graphs, κ decreases sigmoidally with r . In comparison, κ decreases very sharp at low p , which is followed by smooth decay at intermediate p for the anatomical R_{BG} and its randomized networks. It should be noted that all graphs have almost the same κ values.

Functional networks are likely to be denser than anatomical networks, as they will typically contain numerous connections between anatomically unconnected regions [35].

2.4.2 Average Clustering Coefficient

The *average clustering coefficient* C of a network is calculated through individual clustering coefficients C_i of single nodes,

$$C = \frac{1}{n} \sum_{i \in N} C_i = \frac{1}{n} \sum_{i \in N} \frac{2t_i}{k_i(k_i - 1)}. \quad (2.4)$$

where t_i is the number of triangles around node i and k_i is the degree of node i [23]. The clustering coefficient is a measure of segregation, that is, the ability for specialized processing to occur within densely interconnected groups of brain regions [20]. It reveals how the individual nodes in a graph cluster together; how many neighbors of a node are neighbors of each other.

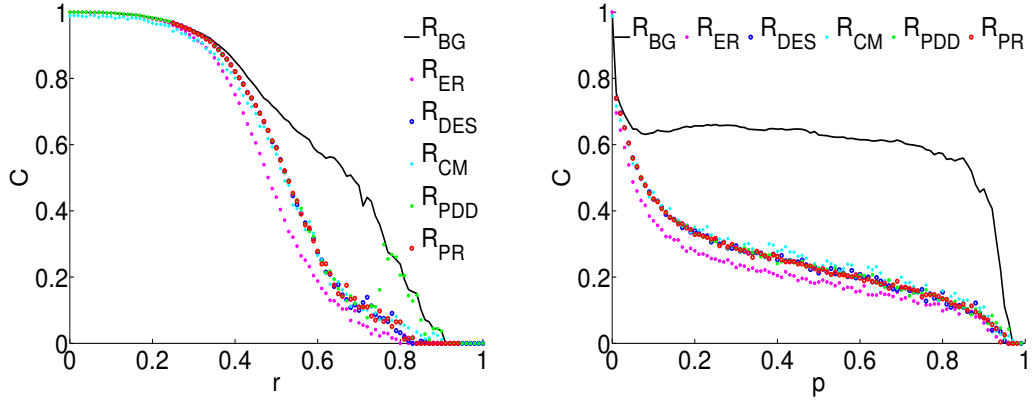


FIGURE 2.11: Average clustering coefficient of the functional (left) and anatomical (right) brain graphs and their randomized networks.

The clustering coefficient C_i of a node i is a measure of local connectivity and is highly correlated with the local efficiency of the information transfer [22]. The C_i is formulated as the ratio of t_i over all possible edges of the node i ; $\binom{k_i}{2}$. The average clustering coefficient C is a normalized version of C_i for the whole network, yielding now a global property. All C values are between 0 and 1. Figure 2.11 shows that at lower binarization thresholds, nodes tend to cluster more due to a higher number of existing edges. The empirically obtained brain networks of FC and AC maps have the highest C compared to random graphs. The local information transfer seems to be more efficient in the brain graphs. The randomized graphs R_{ER} , R_{DES} , R_{CM} , R_{PDD} and R_{PR} (Figure 2.11, right) share more nodes with lower degrees compared to the anatomical R_{BG} .

2.4.3 Transitivity

Transitivity is a similar measure to the clustering coefficient, and also quantifies segregation in the network. It is defined as [24]

$$T = \frac{2 \sum_{i \in N} t_i}{\sum_{i \in N} k_i(k_i - 1)}. \quad (2.5)$$

If a node has links to two other nodes, transitivity inquires whether those two other nodes are also connected to each other. It asks, what percentage of triangles in the network is closed. Transitivity resembles clustering coefficient, however, it is defined only for the whole network rather than single nodes.

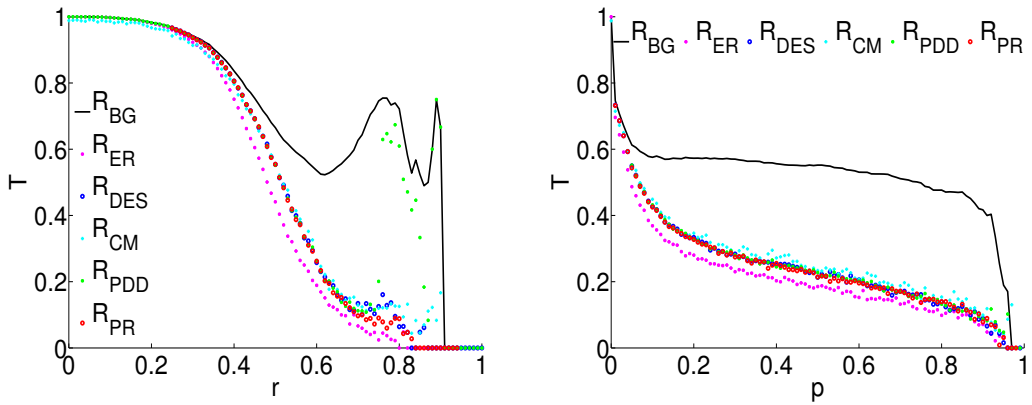


FIGURE 2.12: Transitivity of the brain graphs and random graphs of FCM (on the left) and ACM (on the right).

The degree of transitivity is one of the fundamental differences between real world networks and random networks [17]. This difference is more pronounced than the clustering difference between brain graphs and random graphs, especially for the FC map related graphs when Figures 2.11 and 2.12 are compared. T is more effected by the degree distribution $p(k)$ of a network, the more nodes with lower degrees, the higher the value of T is. AC related graphs tend to have lower $p(k)$ values distributed among many nodes, whereas FC related graphs have higher $p(k)$ values distributed among less nodes. This holds even for R_{BG} and R_{PDD} graphs of FCM in Figure 2.12, and their $p(k)$ is reflected in higher T (Appendix B).

Section 2.4 demonstrated exemplary statistical measures used to identify networks. Other topology measures, i.e. $p(k)$ of networks, assortativity, small-worldness, local and global efficiency, are illustrated in Appendix B. The next section will introduce the modeling approach for the neuronal activity in each brain node.

2.5 FitzHugh-Nagumo Model for Neuronal Activity Simulation

An fMRI-BOLD experiment reveals the correlation coefficients between timeseries of BOLD activity among pre-defined brain regions. The empirical functional connectivity matrix (FCM) derived from fMRI-BOLD technique in this project reflects those coefficients among $N = 90$ AAL regions at the resting state of the human brain, i.e. no stimulus is introduced to the subject. Despite the lack of any stimulus, the observed fMRI-BOLD signal in the mammalian brain is highly structural and robust at low frequency fluctuations (<0.1 Hz) [1, 2, 36]. However, the underlying reason of these well organized spatio-temporal dynamics has not yet been completely resolved. The existing models of resting-brain dynamics hypothesize that functional interactions result from a complex interplay between intrinsic brain dynamics and anatomical connections [8]. This section proposes a modeling approach for the ongoing neuronal activity at the brain's resting state, i.e. how underlying correlated behavior among distant cortical brain regions arises [5]. Once the model is provided with bio-physically plausible parameter ranges with the help of previous studies, the time-series of nodes in brain graphs will be extracted by means of model simulations and compared to randomly constructed networks. Results will be discussed on Chapter 3.

The theoretical model of choice for the neuronal activity is the FitzHugh-Nagumo (FHN) system phenomenologically describing physiological states of nerve membrane potential [37, 38]. The FHN model will be used to represent the neuronal activity of a nerve cell population, in other words, an AAL node in this project. Local dynamics of a single node will then be globalized in the whole brain network via mutual time-delayed interactions among nodes. Here, the time delay Δt_{ij} is assumed to arise from a finite signal propagation velocity v between nodes i and j . Time-delayed interactions are scaled with a coupling strength c [10–12]. Another important parameter for FHN simulations is the threshold r or the probability p , values used to extract adjacency matrices from functional connectivity (FM) and anatomical connectivity (AM) maps of brain at resting state.

The first objective is to investigate plausible c , v , and r or p ranges at which our simulated

neuronal activity of FC and AC related brain graphs is similar to the empirical fMRI-BOLD and DW-MRI data sets (Section 2.2). The FHN model will also be applied to randomly constructed graphs described in Section 2.3. The second objective is to identify such regions in the explored parameter space for which the simulated time-series of the empirically obtained networks are distinguishable from that of randomly constructed graphs. The effects of c , v and r or p as well as the network characteristics of graphs will be taken into consideration. At the end, I aim to gain further insight into the key features of anatomical brain structures by a comparison to randomized networks.

The FHN model is designed to reflect the neuronal activity as a simulated time-series. It does not correspond to the BOLD activity. The objective of the FHN model is the following: the simulated neuronal activity will be used to infer the BOLD signal via the Balloon-Windkessel hemodynamic model as described in the Section 2.6 [6].

Subsections 2.5.1 and 2.5.2 will describe a set of nonlinear differential equations for the FHN local dynamics, carry out a stability analysis, and introduce the effect of a Gaussian white noise on the system. The dynamics of a single node will then be globalized via mutual couplings with a second node and the effect of time-delayed interactions will be demonstrated in Subsection 2.5.3. Subsection 2.5.4 will embed the complete FHN simulation into a simple graph and the first exemplary time-series of a node will be illustrated.

2.5.1 FitzHugh-Nagumo Model Local Dynamics

This section aims to demonstrate the local dynamics of a brain node with the FHN model [37, 38]. Here, the node is assumed to be isolated, meaning that it is not connected to any other node in the brain. The FHN model has an activator variable x and an inhibitor variable y . Their time evolution is represented with the same implementation as in [10, 11] in the following nonlinear differential equations:

$$\dot{x} = \tau \left(y + \gamma x - \frac{x^3}{3} \right) \quad (2.6a)$$

$$\dot{y} = -\frac{1}{\tau}(x - \alpha + by - I), \quad (2.6b)$$

where time scale separation τ denotes the time constant accelerating x and decelerating y , I is the external stimulus parameter and γ , α , b are system parameters. x and

y are considered to be counteracting variables capturing alterations of the membrane potential of a neuronal population of around 10^9 cells. None of the activator or the inhibitor variables include any coupling parameter for the described local activity and additionally I is chosen to be 0 [10].

The *fixed point* (x_f, y_f) of the system is defined such that there is no change in the variables over time $\dot{y} = \dot{x} = 0$. The fixed point condition substituted back into equations (2.6a) and (2.6b) yields a set of *nullcline* equations,

$$y = \frac{x^3}{3} - \gamma x \quad (2.7a)$$

$$x = \alpha - by, \quad (2.7b)$$

where equation (2.7a) will be called y -*nullcline* and (2.7b) x -*nullcline* from now on. The stability analysis is performed by calculating eigenvalues of the *Jacobian Matrix*, \mathbf{J} at the intersection of nullclines, (x_f, y_f) . The linearization of equations (2.6a) and (2.6b) helps to find \mathbf{J} straightforwardly,

$$\begin{pmatrix} \frac{dx}{dt} \\ \frac{dy}{dt} \end{pmatrix} = \begin{pmatrix} \tau(\gamma - x_f^2) & \tau \\ -\frac{1}{\tau} & -\frac{b}{\tau} \end{pmatrix} \begin{pmatrix} x \\ y \end{pmatrix}, \quad (2.8)$$

and therefore:

$$\mathbf{J} = \begin{pmatrix} \tau(\gamma - x_f^2) & \tau \\ -\frac{1}{\tau} & -\frac{b}{\tau} \end{pmatrix}. \quad (2.9)$$

We calculate the determinant and trace of \mathbf{J} as the following:

$$\det \mathbf{J} = b(x_f^2 - \gamma) + 1 \quad (2.10a)$$

$$\text{tr}\mathbf{J} = \frac{1}{\tau} [\tau^2(\gamma - x_f^2) - b]. \quad (2.10b)$$

This allows us to determine the eigenvalues of \mathbf{J} as the following,

$$\det(\mathbf{J} - \lambda \mathbf{I}) = 0 \quad (2.11a)$$

$$\Leftrightarrow \lambda^2 - \lambda \text{tr}\mathbf{J} + \det \mathbf{J} = 0 \quad (2.11b)$$

$$\Rightarrow \lambda_{1,2} = \frac{\text{tr}\mathbf{J} \pm \sqrt{(\text{tr}\mathbf{J})^2 - 4 \det \mathbf{J}}}{2} \quad (2.11c)$$

$$\Rightarrow \lambda_{1,2} = \frac{\tau^2(\gamma - x_f^2) - b \pm \sqrt{(\tau^2(x_f^2 - \gamma) - b)^2 - 4\tau^2}}{2\tau}. \quad (2.11d)$$

The parameters in the FHN model are tuned so that solutions render a damped oscillatory behavior for each node locally; $\alpha = 0.85$, $b = 0.2$, $\gamma = 1.0$ and $\tau = 1.25$ [5]. The solution of the condition $\dot{y} = \dot{x} = 0$ gives coordinates of $(x_f, y_f) = (0.98, -0.67)$, which is calculated numerically here. All parameters plugged in eigenvalue equation (2.11d) results in $\lambda_1 = -0.056 + 0.996i$ and $\lambda_2 = -0.056 - 0.996i$. Since the real parts of both eigenvalues are negative, the fixed point is said to be *stable* and since λ_1 and λ_2 are complex conjugate pairs, the fixed point can be alternatively called a *stable focus*. Variables x and y are expected to relax onto the fixed point over time.

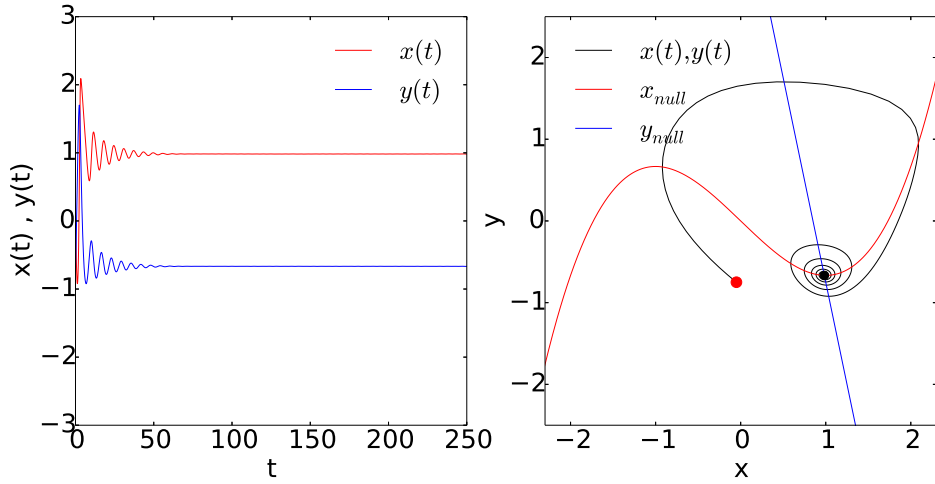


FIGURE 2.13: Local dynamics of an isolated node: time evolution of x and y (left) and nullclines together with $x(t), y(t)$ in state space (right). The fixed point $(x_f, y_f) = (0.98, -0.67)$ is drawn with a black dot at the intersection of nullclines and initial point (x_0, y_0) is illustrated with a red dot. The FHN model parameters are $\alpha = 0.85$, $\gamma = 1.0$, $b = 0.2$, $\tau = 1.25$.

In Figure 2.13, the time evolution of x and y resembles damped oscillations at the beginning. Following a rapid excitation and inhibition, both variables converge to the fixed point. In state space, this relaxation is illustrated as a clockwise trajectory starting from a randomly chosen (x_0, y_0) and falling on (x_f, y_f) with smaller and smaller amplitude oscillations. The system is identified in a quiescent state, or, it is said to be at the onset of instability. The scale of change in x is more pronounced than y due to the time scale separation τ in the FHN model.

2.5.2 Noise Effect

The local dynamics of a node can be extended by additional noise terms,

$$\dot{x} = \tau \left(y + \gamma x - \frac{x^3}{3} \right) + Dn_x \quad (2.12a)$$

$$\dot{y} = -\frac{1}{\tau}(x - \alpha + by - I) + Dn_y, \quad (2.12b)$$

where D is the noise strength, and n_x and n_y represent Gaussian white noise sources with zero mean and unity variance. Neither the coordinates of the fixed point nor the eigenvalues are affected by the noise. However, dynamics of the system goes under a change such that the stability will be effectively lost.

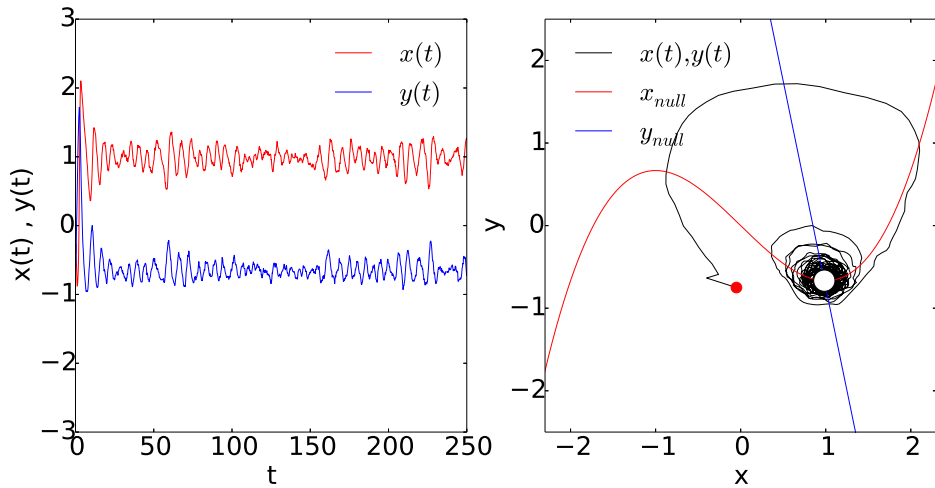


FIGURE 2.14: Local dynamics of two variables x and y with same parameters as in Figure 2.13 Gaussian white noise with strength $D = 0.05$ is added. The fixed point $(x_f, y_f) = (0.98, -0.67)$ is drawn with a white point in state space where two nullclines intersect.

In Figure 2.14, the noise drives subthreshold oscillations as realized in the time evolution of activator and inhibitor. It prevents x and y variables from relaxing on the fixed point, instead, they fluctuate around it.

2.5.3 Coupled Dynamics

This section demonstrates the effect of mutual coupling between two exemplary nodes with FHN model. Now, we consider two nodes connected to each other, either functionally or structurally as in FCM or in ACM (Section 2.1). The effect of this connection is

captured theoretically with a global coupling term and time delayed interactions,

$$\dot{x}_1 = \tau \left(y_1 + \gamma x_1 - \frac{x_1^3}{3} \right) + c[x_2(t - \Delta t_{12})] + Dn_{x1} \quad (2.13a)$$

$$\dot{y}_1 = -\frac{1}{\tau}(x_1 - \alpha + by_1 - I) + Dn_{y1} \quad (2.13b)$$

$$\dot{x}_2 = \tau \left(y_2 + \gamma x_2 - \frac{x_2^3}{3} \right) + c[x_1(t - \Delta t_{21})] + Dn_{x2} \quad (2.13c)$$

$$\dot{y}_2 = -\frac{1}{\tau}(x_2 - \alpha + by_2 - I) + Dn_{y2}, \quad (2.13d)$$

where c is the coupling strength, subindices 1 and 2 stand for corresponding nodes, Δt_{12} and Δt_{21} are time delays required for coupled node interactions and D is the Gaussian white noise strength. For simplicity, the global dynamics are illustrated with same local parameters as before, while time delays are taken to be homogeneous, $\Delta t_{12} = \Delta t_{21} = 0.5$.

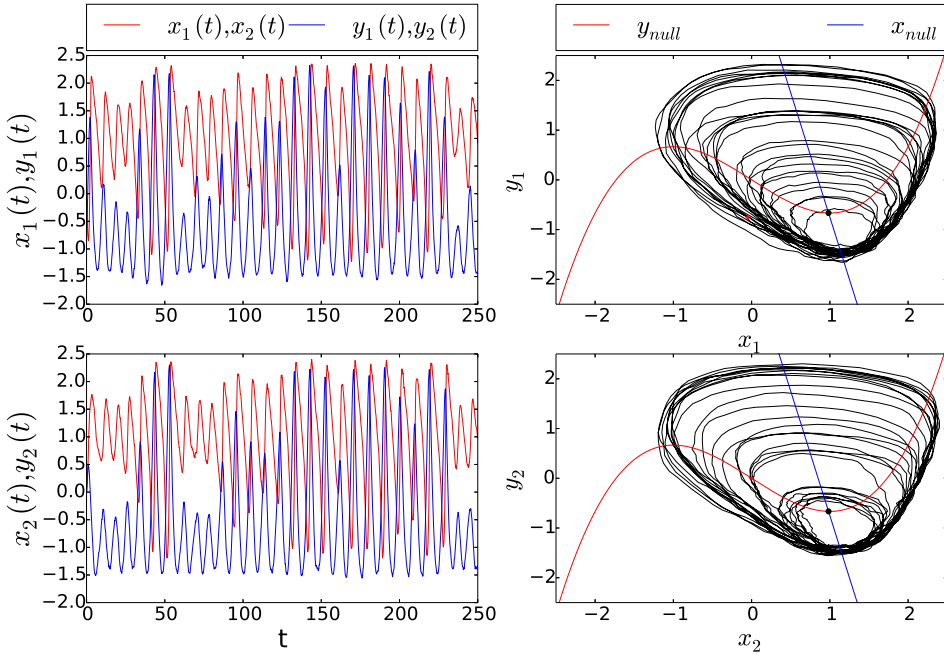


FIGURE 2.15: FHN global dynamics of two nodes with variables x_1, y_1 (at upper left) and x_2, y_2 (at lower left), parameters of the model $\alpha = 0.85$, $\gamma = 1.0$, $b = 0.2$, $\tau = 1.25$, $D = 0.05$, $c = 0.5$ and $\Delta t_{12} = \Delta t_{21} = 0.5$. The fixed point is the same for both systems $(x_f, y_f) = (0.98, -0.67)$, it is drawn with a black dot at the intersection of nullclines in state space.

Figure 2.15 illustrates temporal dynamics of a functionally interacting node pair; over time (left) and in state space (right). The mutual coupling between nodes pushes both

systems (x_1, y_1) and (x_2, y_2) to be oscillatory with visibly larger amplitudes in comparison to local dynamics and noise effect in Figures 2.13 and 2.14. The system does not settle down to the fixed point anymore, indicating loss of the stability.

2.5.4 Network Dynamics

After introducing the local and global dynamical models of nodes, the final version of FHN model to be simulated as the neuronal activity in the complete brain graph or random network is denoted with the following notation [5],

$$\dot{x}_i = \tau \left(y_i + \gamma x_i - \frac{x_i^3}{3} \right) - c \sum_{j=1}^N a_{ij} x_j(t - \Delta t_{ij}) + D n_x \quad (2.14a)$$

$$\dot{y}_i = -\frac{1}{\tau} (x_i - \alpha + b y_i - I) + D n_y, \quad (2.14b)$$

where the index i represents any node among $N = 90$ AAL regions, c is coupling strength, a_{ij} is the adjacency matrix (AM), $i, j = 1, \dots, N$. This is the crucial link between network analysis part and FHN section. If nodes are connected in a given network, then $a_{ij} = 1$, otherwise $a_{ij} = 0$. Δt_{ij} is the time delay factor arising from finite signal propagation velocity v among nodes. Δt_{ij} is calculated as $\Delta t_{ij} = \frac{d_{ij}}{v}$ [10–12], where d_{ij} is the matrix of Euclidean distances between centers of brain regions from which BOLD time series are extracted [39] (see Appendix C for d_{ij}). The external stimulus is again set to zero $I = 0$. The noise (n_x, n_y) factors are Gaussian white noise sources, the strength of noise is $D = 0.05$.

The time delay coupled set of ordinary differential equations is solved numerically with PYTHON-module PYDELAY-algorithm (<http://pydelay.sourceforge.net>) based on Bogacki-Shampine method [40, 41]. Let us introduce two sample graphs having different network topology (Figure 2.16) and model the temporal dynamics of nodes with FHN dynamics (Figure 2.17).

In Figure 2.16, links represent functional connections between node pairs: For instance, node 1 has no edge on the left, and it is then connected to 3 nodes on the right. Both graphs are simulated with the FHN model. Figure 2.17 visualizes the extracted time-series of node 1; $k_1 = 0$ (top) and $k_1 = 3$ (bottom). Its dynamical view for $k_1 = 0$ is

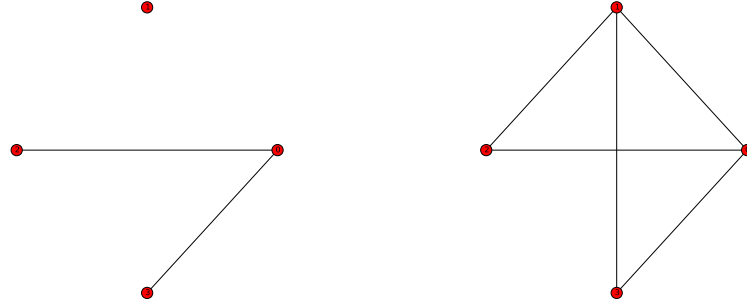


FIGURE 2.16: Two sample graphs to be simulated with FHN model, the upper-most node, say node 1 is not connected at all in first graph (left) and connected by 3 edges in second graph (right).

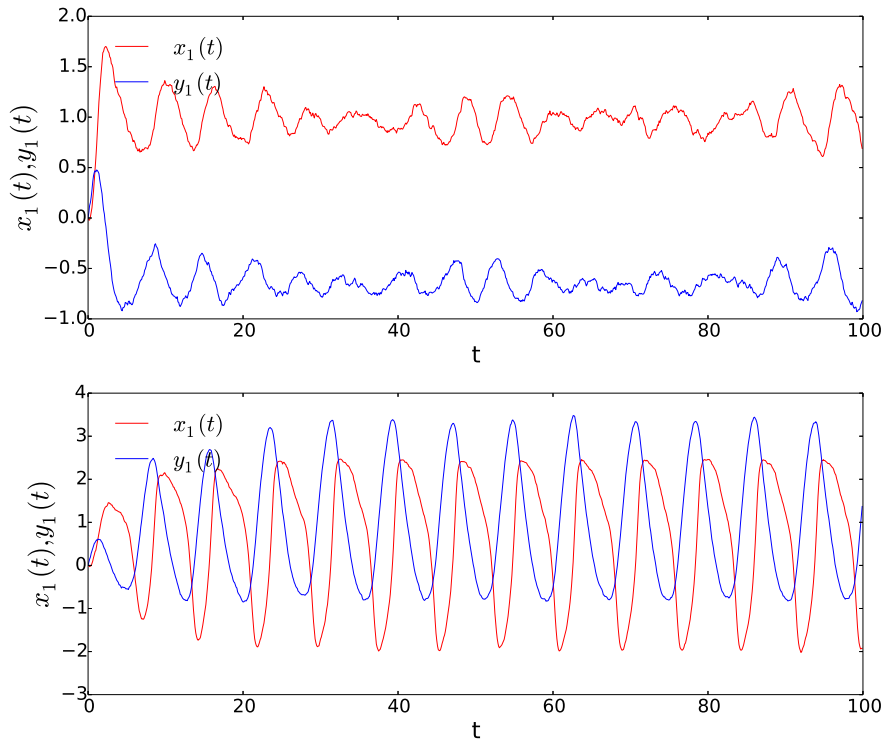


FIGURE 2.17: Analogous time-series of node 1 chosen from graphs illustrated in Figure 2.16. Time-series at top is of the unconnected node 1 ($k_1 = 0$, Figure 2.16, left), at down is of 3-edge connected node 1 ($k_1 = 3$, Figure 2.16, right). FHN parameters are $\alpha = 0.85$, $\gamma = 1.0$, $b = 0.2$, $\tau = 1.25$, $D = 0.05$, $\Delta\tau_{ij} = \frac{d_{ij}}{v}$, where an arbitrary d_{ij} is used for corresponding sample graphs in Figure 2.16 for visualization purpose.

in agreement with FHN local dynamics with noise effect (Figure 2.14). However, when it is connected to by 3 edges, then large scaled oscillatory patterns of its activator and inhibitor variables can be observed as a consequence of global coupling terms.

This section described the chosen theoretical model for the neuronal activity. The next step is to study the introduced neuronal dynamics on empirically derived and randomly constructed graphs. $N = 90$ nodes in any given network will be simulated with the complete FHN timeseries notation for 7.5 minutes. A 90×90 correlation matrix will be used for each FHN simulated network. Then, Pearson correlation coefficients between simulated timeseries of node pairs will be calculated for one graph.

The FHN model is involved in crucial steps in this Master's project: parameter analysis, distinguishing brain graphs and random graphs and finally extracting BOLD activity. Simulations on brain graphs obtained from FCM and ACM matrices will be compared to the original fMRI-BOLD data in parameter spaces by tuning three parameters in bio-physically plausible ranges: coupling strength c and velocity v as well as a threshold r or probability p value, which is used while constructing adjacency matrices a_{ij} of given graphs. Simulations on random graphs will be used to identify regions in the explored parameter space for which the empirical data differ from that of the random graphs. Not only the effect of tuned parameters c , v and r or p , but also the contribution of topological measurements of graphs will be taken into account. The modeled neuronal activity oscillates dominantly at high frequency ranges (> 20 Hz). However, the BOLD fluctuations measured with fMRI are ultra slow (< 0.1 Hz). In order to capture the BOLD signal, FHN time-series of brain graphs will be simulated further with another theoretical model, which will be introduced in the next session.

2.6 Balloon-Windkessel Model for BOLD Activity Simulation

Blood oxygen level dependent (BOLD) contrast imaging is one of the underlying mechanisms of fMRI to map brain activity at resting state. A BOLD signal is thought to arise from interactions between neuronal activity and regional changes in the surrounding of those active neurons such as blood volume, blood flow and oxygen level in capillaries. When neuronal activity increases, the blood flow in blood vessels surrounding this

neuronal region rises, causing a change in relative amounts of deoxygenated and oxygenated forms of Hemoglobin (dHB and Hb). The difference in magnetic properties of dHB (paramagnetic) and Hb (diamagnetic) is the key ingredient to the observed changes in the magnetic resonance signal. A better understanding of the resting-state BOLD signal is required to better interpret neuronal activity. The previous section already proposed a model for the neuronal activity, the FHN model. This section will introduce a hemodynamic process to capture BOLD activity with a mathematical model known as the Balloon-Windkessel model [42].

In addition to the variations in magnetic properties of the blood caused by blood flow in vessels, there are other physiological changes during alteration in neuronal activity that affect the temporal dynamics of BOLD signal, i.e. cerebral blood flow (CBF), cerebral blood volume (CBV) and cerebral metabolic rate of oxygen consumption (CMRO₂). Moreover, the BOLD response is subject dependent: the physiological baseline state of the individual under examination is used to scale its BOLD response, which makes it difficult to interpret the BOLD signal when the baseline state varies [43]. Moreover, the sensitivity of a BOLD signal to variations in vascular and metabolic physiology complicates an accurate interpretation. The biophysical descriptions of the BOLD signal are still not fully satisfactory for the resting state.

Changes in the BOLD signal obtained in an fMRI experiment represent an indirect measure of underlying neuronal activity [7]. The modeled neuronal activity can be used to infer the BOLD signal observed in the fMRI data via the Balloon-Windkessel hemodynamic process, which mediates between a non-linear timeseries and all the measured BOLD response [6]. In short, the Balloon-Windkessel model picks an input signal from neuronal activity timeseries and generates the BOLD activity timeseries as a function of changes in CBF, CBV, CMRO₂. The main input of the Balloon-Windkessel model is a neuronal signal in the form of either a spiking rate or a local field potential [44]. The neuronal signal in this project will be the normalized FHN time-series of an activator variable, which describes the excitatory membrane potential dynamics of a neuronal population.

The study of Friston et al. shows that it is possible to capture ultra-slow frequency oscillations (< 0.1 Hz) in the hemodynamic process, given a higher frequency neuronal

input for event related responses [6]. Here, the same model will be tested for the resting-state activity to find out whether it is possible to extract BOLD activity from FHN-modeled $N = 90$ AAL brain nodes. Each brain graph obtained from FCM and ACM data sets will be embedded into the Balloon-Windkessel model, and a parameter analysis will be carried out while comparing resultant BOLD simulations to the fMRI-BOLD empirical data set.

2.6.1 Hemodynamic Model

This section is designed to review the Ballon-Windkessel hemodynamic model introduced in Friston et al [6].

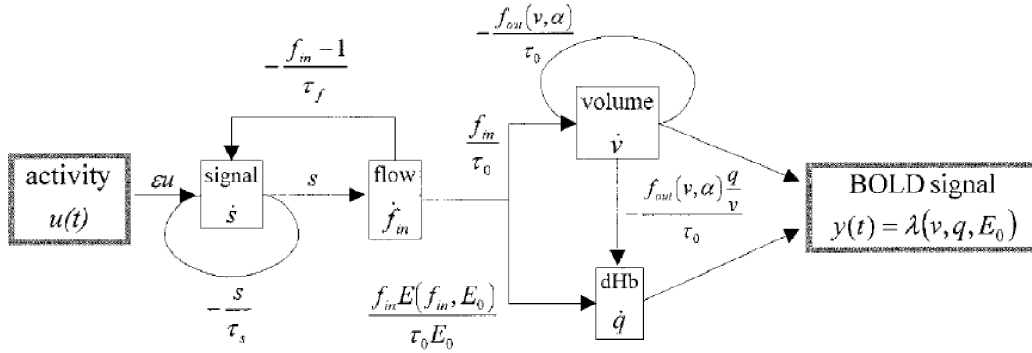


FIGURE 2.18: The hemodynamic model for the BOLD activity illustrated in Friston et al. [6]

TABLE 2.2: Notations and their brief descriptions for hemodynamics in Friston et al.

Abbreviation	Description
$u(t)$	nonlinear input signal
s	blood-flow inducing signal
τ_s	time constant of s
f_{in}	CBF (inflow)
τ_f	feedback time constant
v	CBV
τ_0	mean transit time of v
α	stiffness exponent
$f_{out}(v, \alpha)$	CBF (outflow)
E_0	resting net O_2 extraction rate
$E(f_{in}, E_0)$	fraction of O_2 extracted from f_{in}
q	dHb content in voxel
$y(t)$	output BOLD signal

The following set of equations describe the Balloon-Windkessel model;

$$\dot{s} = \epsilon u(t) - \frac{s}{\tau_s} - \frac{f_{in} - 1}{\tau_f} \quad (2.15a)$$

$$\dot{f}_{in} = s \quad (2.15b)$$

$$\dot{v} = \frac{f_{in}}{\tau_0} - \frac{f_{out}(v, \alpha)}{\tau_0} \quad (2.15c)$$

$$\dot{q} = \frac{f_{in}E(f_{in}, E_0)}{\tau_0 E_0} - \frac{f_{out}(v, \alpha) q}{\tau_0 v} \quad (2.15d)$$

with the functions:

$$f_{out}(v, \alpha) = v^{1/\alpha} \quad (2.16a)$$

$$E(f_{in}, E_0) = 1 - (1 - E_0)^{1/f_{in}}. \quad (2.16b)$$

Finally, the output BOLD signal is modeled as a function depending on variables v , q and parameter E_0 ,

$$y(t) = \lambda(v, q, E_0) = V_0 \left[k_1(1 - q) + k_2 \left(1 - \frac{q}{v} \right) + k_3(1 - v) \right], \quad (2.17)$$

where $k_1 = 7E_0$, $k_2 = 2$, $k_3 = 2E_0 - 0.2$, and V_0 is the resting blood volume fraction. The set of differential equations for \dot{s} , \dot{f}_{in} , \dot{v} , \dot{q} is numerically integrated using Euler's method with step size $dt = 10^{-3}$. The six unknown parameters ϵ , α , τ_0 , τ_f , τ_s and E_0 are picked up from standard ranges given in Friston et al [6].

The CBF is denoted by two symbols based on its flow direction: f_{in} and f_{out} , venous blood inflow and outflow, respectively. The nonlinear neuronal activity $u(t)$ and f_{in} are thought to trigger the blood flow inducing signal s . Equation (2.15a) above represents time-dependent change of s depending on $u(t)$, f_{in} and s . The three system parameters ϵ , τ_s and τ_f are described as following: an efficacy parameter for $u(t)$ to raise s , a time constant for decay of s , and another time constant for autoregulatory feedback from CBF, respectively [45, 46].

Hemodynamics in the brain assumes that alterations in regional CBF are shaped by an underlying neuronal activity. Equation (2.15b) above presents the rate of change of f_{in} with a linear transformation of s , which can originate from a nonlinear neuronal activity model [47, 48].

The alteration in cerebral blood volume v is formulated by subtracting f_{out} from f_{in} , both rated physiologically with a time constant τ_0 , which is also referred to as *mean transit time* [49]. The Windkessel model contributes to the brain hemodynamics while modeling CBF through CBV: equation (2.16a) describes a function for f_{out} depending on v and a parameter α (the *stiffness exponent*) [49].

The change in magnetic properties of blood is expressed with the difference between dHb uptake and release. The dHb uptake is proportional to the blood inflow f_{in} to the venous compartment and available oxygen to be coupled to Hb. The amount of oxygen carried with blood inflow is estimated with a function $E(f_{in}, E_0)$ divided by resting net oxygen extraction rate E_0 as given in equation (2.16b) [42]. The dHb release is proportional to the blood outflow f_{out} and the concentration of dHb in corresponding voxel volume v .

In summary, Chapter 2 described the empirical data sets and methods drawn from nonlinear and network science. Section 2.1 introduced FC and AC maps derived from fMRI-BOLD and DW-MRI measurements, respectively. Section 2.2 presented how to build real brain networks given FC and AC maps of resting-state. Section 2.3 explained the construction of random graphs. Section 2.4 compared the network topology of brain graphs to that of random networks. Section 2.5 and Section 2.6 demonstrated the modeled temporal dynamics for the neuronal activity and BOLD fluctuations in the brain. Chapter 3 will illustrate our results obtained from all introduced methods combined with the experimental data sets.

Chapter 3

Results

The functional connectivity (FC) map is derived from fMRI-BOLD technique and it reveals the BOLD fluctuation correlations between any two AAL regions. The anatomical connectivity (AC) map is obtained from DW-MRI measurement and it represents the probability of any two AAL region to be connected by nerve fibers. (see Section 2.1 for FCM and ACM, Appendix A for AAL describtions). Both data sets are derived at the resting-state activity of human brain, i.e. in the absence of any stimulation.

The brain graphs are constructed in two category: via binarizing FC at different threshold r values and binarizing AC maps at varying p values (Section 2.2). Several randomization procedures are implemented to generate random networks by manipulating FC and AC related brain graphs (2.3). The network topology of all graphs are characterized by statistical measures (Section 2.4, Appendix B).

The neuronal activity of of an AAL region is modeled with the FitzHugh-Nagumo model (Section 2.5) [5, 11]. The BOLD activity is then inferred via the Balloon-Windkessel model (Section 2.6) [6]. All brain and random graphs are firstly simulated with FHN model, their extracted time-series are then used to implement the BOLD activity. The research proposals are to investigate *i*) whether the BOLD dynamics of resting-state can be captured through the AC map of brain and *ii*) if the temporal dynamics of brain graph is distinguishable than that of random networks.

This section categorizes all results in three parts: neuronal activity simulations, BOLD activity simulations and comparison of brain graphs to randomly constructed graphs. In Section 3.1, FHN network model simulated on brain graphs of FC and AC maps are

compared to fMRI-BOLD data and DW-MRI data, respectively. In Section 3.2, the Balloon-Windkessel model applied to neuronal time-series based on brain graphs of FC and AC maps are compared to the single empirical brain map, the fMRI-BOLD data. In Section 3.3, random graphs are simulated with FHN model. The last part aims to illustrate whether or not these random networks can be distinguished from brain graphs in terms of the modeled neuronal activity.

3.1 Neuronal Activity Simulations

3.1.1 Functional Brain Graphs Compared to fMRI-BOLD Data

The adjacency matrices (AM) are constructed via binarizing the fMRI-BOLD data at threshold $r = [0.54, 0.66]$, an exemplary illustration is given in Figure 2.3, Section 2.2. An AM obtained from fMRI-BOLD data represents whether or not any pair of AAL nodes is functionally connected above a defined r . The automated anatomical labeling (AAL) of all $N = 90$ nodes can be reviewed in Table A.1, Appendix A. The brain graph constructed on the AM for given r -values are simulated with FHN network model (Section 2.5).

This section aims to investigate the temporal dynamics of the neuronal activity in human brain by comparing simulated network to the fMRI-BOLD data. The comparisons are carried to parameter spaces of (r, v) and (r, c) , where v is the signal propagation velocity and c is the coupling strength [5, 11].

Once the FHN simulated time-series of all nodes in a brain graph are extracted, the correlation of simulated neuronal activity between any node pairs i, j is quantified by Pearson's correlation coefficient $\rho_{i,j}$,

$$\rho_{i,j} = \frac{\langle u_i(t)u_j(t) \rangle - \langle u_i(t) \rangle \langle u_j(t) \rangle}{\sigma(u_i(t))\sigma(u_j(t))} \quad (3.1)$$

where $u_i(t)$ denotes the FHN time-series of the corresponding node i , σ stands for standard deviation and $\langle \cdot \rangle$ represents the temporal average. Figure 3.1 demonstrates excitatory FHN dynamics of two pairs of nodes. Simulated neuronal time-series of nodes

45 and 28 are well correlated ($\rho_{45,28} = 0.88$, Figure 3.1, top), whereas that of nodes 90 and 87 are poorly correlated ($\rho_{90,87} = 0.13$, Figure 3.1, bottom).

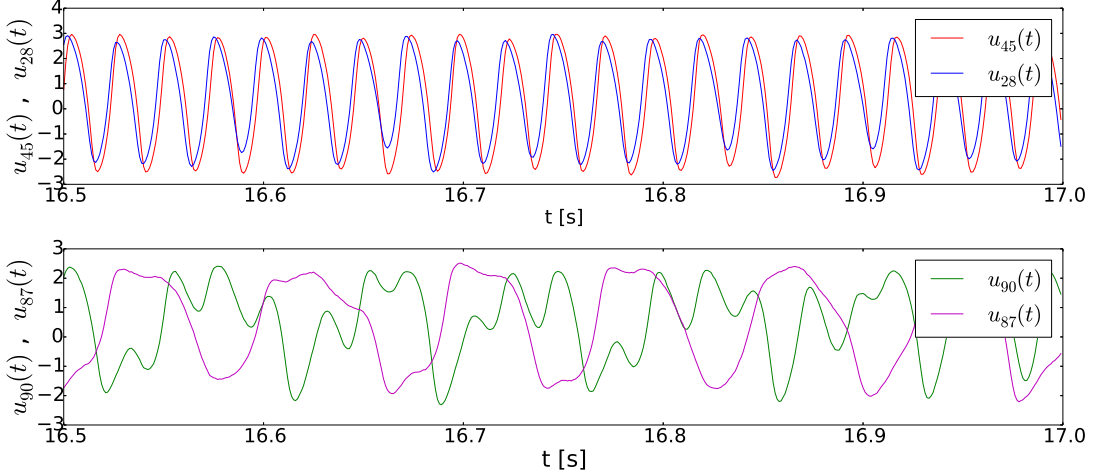


FIGURE 3.1: Temporal dynamics of highly (top, $\rho_{45,28} = 0.88$) and poorly (bottom, $\rho_{90,87} = 0.13$) correlated node couples with FHN model. The simulation parameters are $c = 0.2$, $v = 7$ m/s, $r = 0.60$.

All $\rho_{i,j}$ values among any possible pairwise combination of $N = 90$ nodes are then used to built a 90×90 matrix, which is referred to as simulated correlation matrix (CM). The fMRI-BOLD data was in fact used to obtain a functional correlation matrix (FCM). (Figure 2.1, Section 2.1). Figure 3.2 illustrates a simulated CM and the empirical FCM together for a better visualization. Each colored square represents how strong any pair of nodes i and j addressed on x - and y -axes are correlated in terms of *i*) their temporal dynamics for the simulated CM, *ii*) their BOLD fluctuations for empirical FCM. Colorbars denote $\rho_{i,j}$ -values.

In order to compare the modeling approach to the empirical result, both correlation matrices are compared statistically with Pearson's correlation coefficient, the same linear pairwise correlation method again. All correlation values $\rho_{e,s}$ between empirical e and simulated s data matrices are placed on the parameter spaces. Here, the parameter spaces are designed over (r, v) and (r, c) as seen in Figure 3.3. The purpose is to explore the most promising values for three tuning parameters: r , which defines the topology of AM, the coupling strength c and signal propagation velocity v , which are parameters of the FHN model as explained in Section 2.5. Each color coded square in Figure 3.3 corresponds to one $\rho_{e,s}$ value. Hot colors represent high correlation between simulated

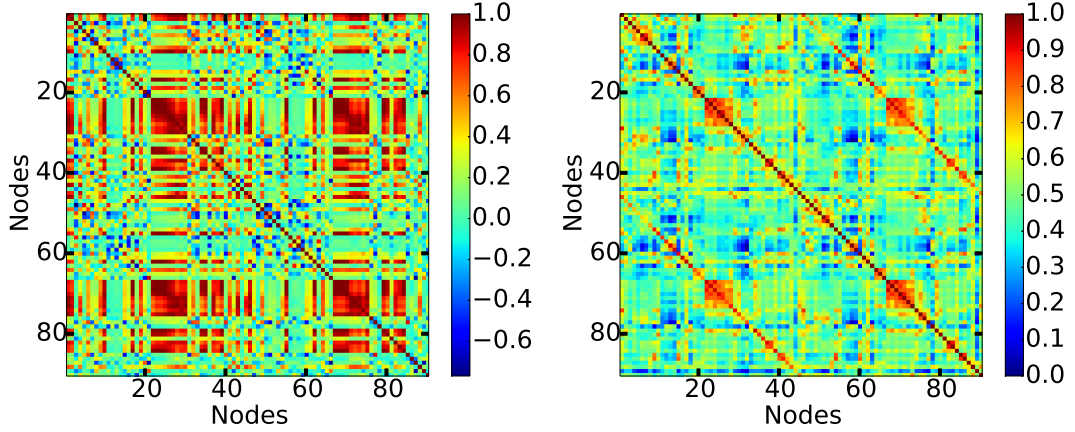


FIGURE 3.2: Simulated CM obtained from FHN network simulations (left) and empirical FCM (right). The parameters of CM are $c = 0.2$, $v = 7$ m/s, $r = 0.60$, overall correlation between two matrices is $\rho_{e,s} = 0.43$

and empirical data, 0 means no correlation at all and cold colors below zero points out anti-correlations.

A correlation value close to 1 in FCM indicates that the quantified functional activities of corresponding nodes in the right and left hemisphere highly resemble each other, see subdiagonals in Figure 3.2 (right). The AAL regions tend to be correlated at $\rho_{i,j} = 0.5$ in FCM. The simulated CM exhibit in general either higher correlations or anti-correlations, see Figure 3.2 (left). The traces of subdiagonals in FCM can be observed slightly on the simulated CM. The overall correlation between CM and FCM is $\rho_{e,s} = 0.43$.

It can be inferred from Figure 3.3 that fast signal propagation velocity v above 6 m/s, a low r in the range of $[0.54, 0.60]$ and a coupling strength c around $[0.1, 0.4]$ would result in high correlations between simulated and empirical data sets. The v -value range was already shown to be around 7 m/s in the previous studies [5, 11]. The network topology of the brain graphs constructed via AM's is characterized for r -values, i.e. $0.54 \leq r \leq 0.60$ corresponds to a network density $0.35 \geq \kappa \geq 0.18$ (Section 2.4.1). Beyond $r > 0.60$, less densely connected brain networks exhibit dramatically changing transitivity T , shortest pathway d_{ij} , small worldness S and assortativity A (Section 2.4 and Appendix B) and simulations become distinctly different from experiment.

Figure 3.4 concludes this section with a fast Fourier transform analysis over all nodes given in Figure 3.2. The z -axis of 3D plot has a natural logarithmic scale in order to magnify the frequency power spectrum values. The FHN model results mostly in very

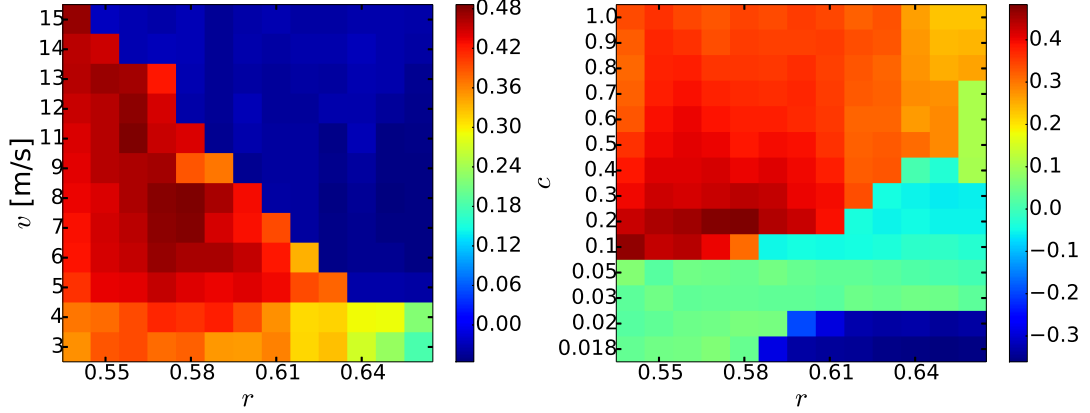


FIGURE 3.3: Analogy between FHN network model simulated brain graphs obtained from FC map and fMRI-BOLD result in parameter spaces (r, v) (constant coupling strength $c = 0.2$, left) and (r, c) (constant velocity $v = 7 \text{ m/s}$, right). The colorbars stand for $\rho_{e,s}$.

fast oscillations around 20 Hz, 40 Hz and 58 Hz quite uniform. The slow oscillatory component peaks around 0.1 Hz. The BOLD fluctuations are ultra slow scaled oscillations ($< 0.1 \text{ Hz}$), and FHN network model is not capable of capturing the BOLD activity. All extracted neuronal time-series will be used to implement the BOLD dynamics later in Section 3.2.

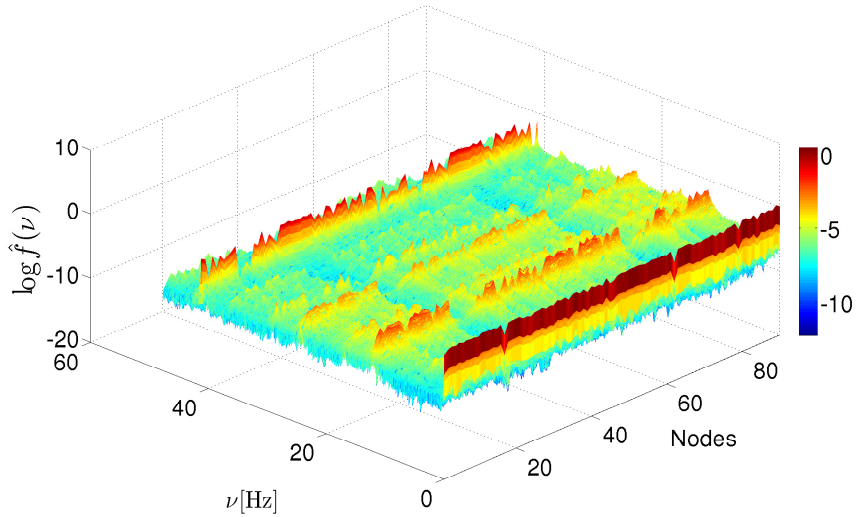


FIGURE 3.4: Illustration of fast Fourier transform of neuronal activity oscillations corresponding to $N = 90$ nodes in simulated CM with parameters given in Fig.3.2.

The next subsection will cover the FHN network model simulation results obtained from the anatomical brain graphs. The statistical comparison of temporal dynamics of node

pairs as well as the comparison of simulated and empirical data will be quantified with the same methodology: the Pearson's correlation coefficients.

3.1.2 Anatomical Brain Graphs Compared to DW-MRI Data

The adjacency matrix (AM) used in this subsection are constructed via binarizing the anatomical connectivity (AC) map at probability $p = [0.18, 0.82]$. AC map used in this project is obtained from the DW-MRI technique at resting-state of brain, which reveals the probability of any two AAL regions to be structurally connected with the fiber tracks (Section 2.1). The AAL nodes refer to the same cortical and sub-cortical regions used in fMRI-BOLD data extraction (Appendix A). The AM constructed via ACM represents whether or not any pair of nodes i, j is structurally connected above a given p (Section 2.2).

Investing the temporal properties of the brain's AC map is done within the same methodological order as in the previous section. AM's obtained at different p are simulated with the FHN network model, neural time-series $u(t)$ of each node is extracted and Pearson correlation coefficients $\rho_{i,j}$ of temporal dynamics between all pairwise combinations of nodes i, j are calculated. For each FHN network model simulated on AM, a 90×90 matrix is built with calculated $\rho_{i,j}$ values. This matrix is referred to as simulated correlation matrix (CM). The simulated CM's are then compared to the empirical ACM by pairwise Pearson's correlation coefficients $\rho_{e,s}$. The results are carried in to (p, v) and (p, c) parameter spaces. p will lead us to interpret the network topology of the brain graph. The signal velocity along the axons v and the coupling strength c will be used as tuning parameters of FHN model as inspired from the previous studies [5, 11]. This subsection begins from a broad manner by demonstrating $\rho_{e,s}$ -values in parameter spaces, and goes narrower into node dynamics.

Figure 3.5 illustrates Pearson coefficients $\rho_{e,s}$ between experimental e and simulated s correlation matrices in parameter spaces. Highest correlation regime is captured at $4\text{m/s} < v < 8\text{m/s}$, $0.1 < c \leq 0.5$ with $0.18 \leq p \leq 0.70$. The network density of brain graphs based on AC map is $0.35 \geq \kappa \geq 0.18$ for the corresponding $0.18 \leq p \leq 0.70$ (Section 2.4.1). The pattern of $\rho_{e,s}$ -values in Figure 3.5 and Figure 3.3 (Section 3.1.1) resembles each other.

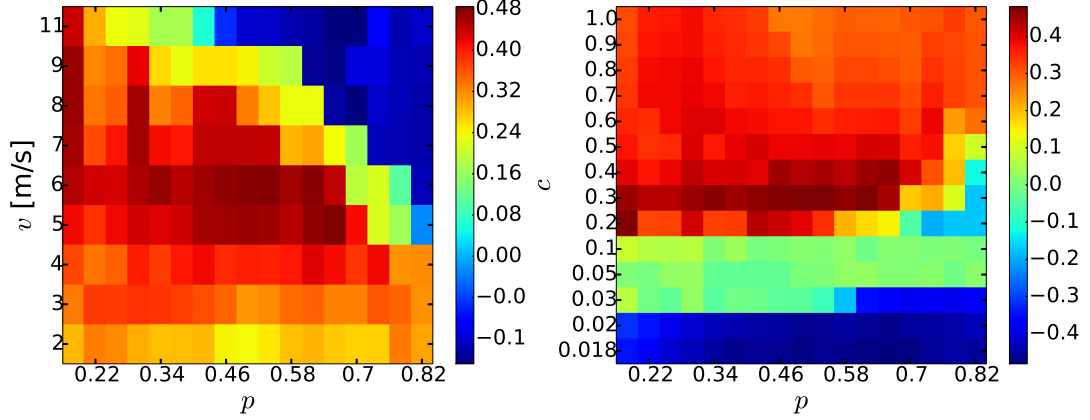


FIGURE 3.5: Analogy between FHN network model simulated brain graphs derived from AC map and DW-MRI result in parameter spaces (r, v) (constant coupling strength $c = 0.3$, left) and (r, c) (constant velocity $v = 6$ m/s, right). The colorbars stand for $\rho_{e,s}$.

p of ACM's lies in a broader range than r of FCM's, when Figure 3.5 is compared to Figure 3.3. The network measures of AC map based brain graphs change smoothly with $0.18 < p < 0.82$, whereas that of FC map related brain graphs change sharply with $0.18 < r < 0.82$. This is why larger steps binarization steps by amount of 0.4 are used. However, at $p > 0.82$ AC map related brain networks tend to have sudden changes in transitivity T , shortest pathway d_{ij} , small worldness S and assortativity A . (All network measures related to the brain graphs can be reviewed through Section 2.4 and Appendix B.)

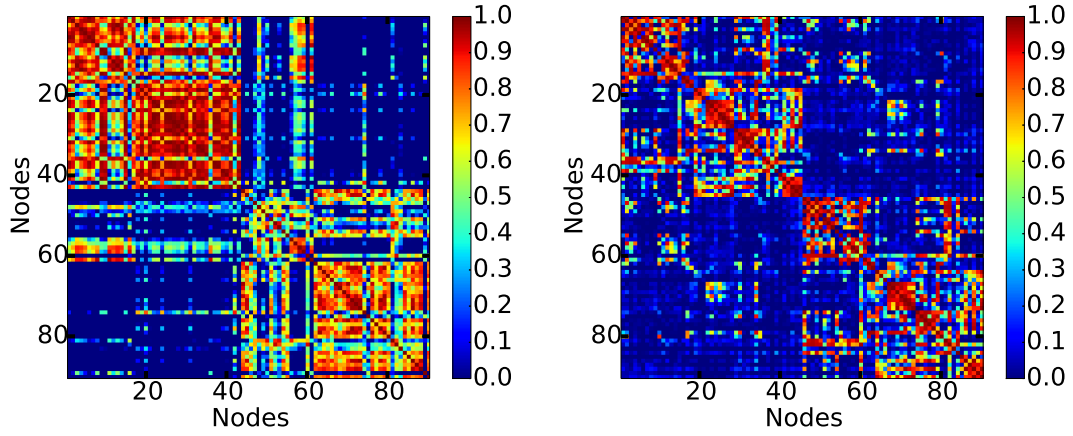


FIGURE 3.6: Simulated CM obtained from FHN network simulations (left) and empirical FCM (right). The parameters of CM are $c = 0.3$, $v = 6$ m/s, $r = 0.50$, overall correlation between two matrices is $\rho_{e,s} = 0.43$

Figure 3.6 illustrates a simulated CM (left) together with the empirical ACM (right).

The simulated CM is chosen from the red-colored squares in Figure 3.5, for instance, the illustrated matrices in Figure 3.6 has a correlation value of $\rho_{e,s} = 0.43$. The hot colors in the simulated CM present highly correlating node pairs in terms of their simulated neuronal time-series, whereas the cold colors express poor correlations. It should be noted that only the excitator variable x of FHN model is considered to quantify correlations (Section 2.5). The colorbar of the empirical ACM denotes the probability p values of two nodes to be connected via nerve fibers.

Figure 3.6 indicates that the nodes in the same hemispheres are more probably to be connected via fiber tracts, see two dominating subsquares in the empirical ACM. The FHN network model simulated on the anatomical brain graph yields also highly correlated temporal activities for the nodes in the same sphere, see subsquares in the simulated CM. However, the correlations of neuronal time-series in CM tend to be more pronounced in comparison to the anatomical connectivity probabilities in the empirical ACM. Although some node pairs are not structurally connected at all, they are captured to be functionally connected via their extracted FHN time-series.

Choosing one red square and one blue square from the simulated CM in Figure 3.6, the simulated time-series of highly and poorly synchronizing node pairs are visualized in Figure 3.7. The modeled temporal dynamics of nodes 43 and 31 are highly correlated, $\rho_{43,31} = 0.86$, whereas that of nodes 90 and 83 are poorly correlated $\rho_{90,83} = 0.15$.

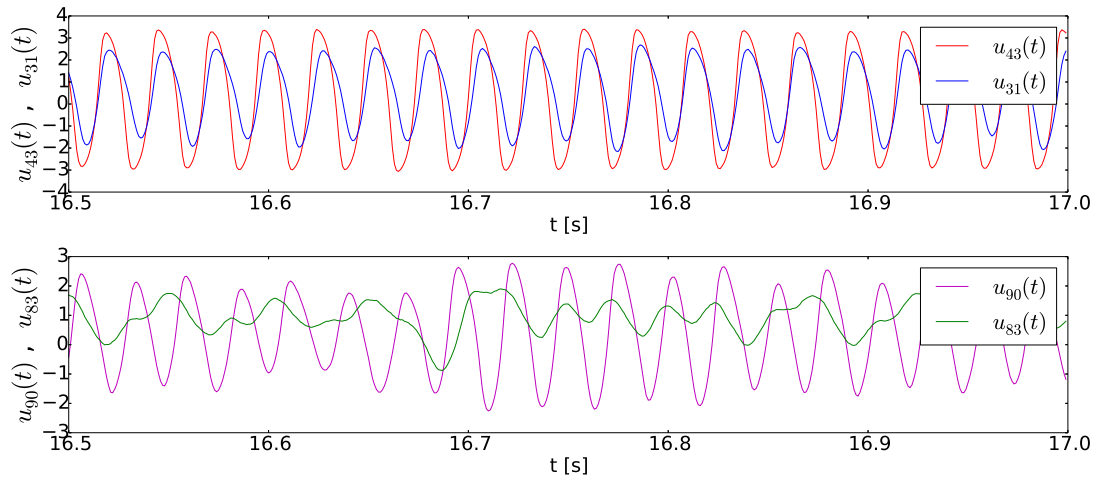


FIGURE 3.7: Temporal dynamics of highly (top, $\rho_{43,31} = 0.86$) and poorly (bottom, $\rho_{90,83} = 0.15$) correlated node couples with the FHN model. The simulation parameters are $c = 0.3$, $v = 6$ m/s, $r = 0.50$.

Finally, a fast Fourier transform (FFT) is carried out to identify the dominating frequency ν -ranges of the FHN network model oscillations. All $N = 90$ nodes of the simulated CM given in Figure 3.6 (left) are analyzed with FFT in Figure 3.8. The temporal dynamics of the nodes are fast oscillatory at $40 \text{ Hz} < \nu < 60 \text{ Hz}$, a slow oscillatory peak is observed around $\nu = 0.1[\text{Hz}]$. The frequency scale of oscillations are in agreement in Figures 3.8 and 3.4. However, the scale of BOLD fluctuations is extremely small compared to the modeled temporal dynamics.

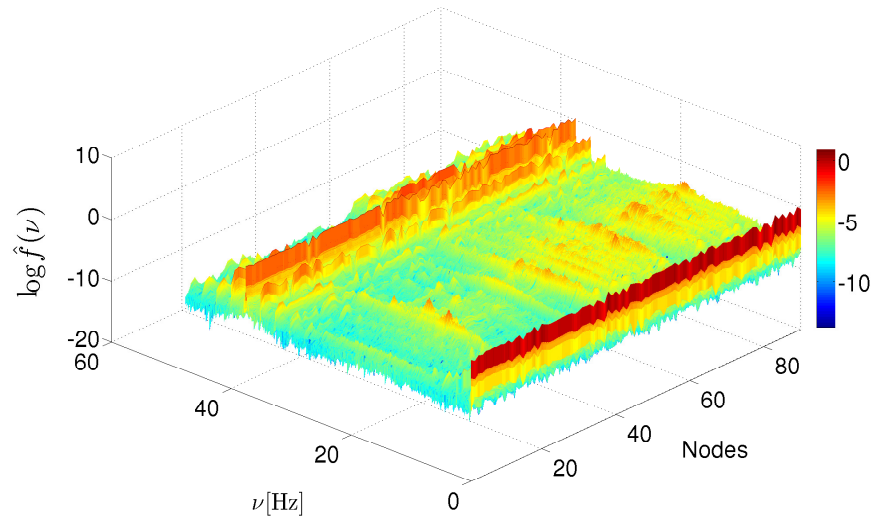


FIGURE 3.8: Illustration of fast Fourier transform of neuronal activity oscillations corresponding to $N = 90$ nodes in simulated CM with parameters given in Figure 3.6.

Up to here, the neuronal activity model of human brain at the resting-state is built on FitzHugh-Nagumo oscillatory network model as previously proposed in [5, 11] (Section 2.5). This model is applied to the adjacency matrices obtained from functional and structural connectivity maps, which are derived from fMRI-BOLD and DW-MRI measurements, respectively. Each FHN network model simulated brain graph (derived from FC and AC maps) compared to their original data sets (empirical FCM and ACM). High correlations between the FHN network model simulations and experimental data sets are captured on parameter spaces by tuning model parameters of c and v , as well as network topology parameter p or r [5, 11]. The next step is to model the low frequency oscillating BOLD activity ($< 0.1 \text{ Hz}$) of resting-state by using the extracted neuronal time-series. The next section will demonstrate the modeled BOLD activity by using these neuronal time-series.

3.2 BOLD Activity Simulations

Blood oxygen level dependent (BOLD) contrast imaging is one of the underlying mechanisms of fMRI to map the functional activity correlations among brain regions at the resting-state. The existing models of resting-state brain dynamics hypothesize that functional interactions result from a complex interplay between intrinsic brain dynamics and underlying structural connections [8]. One of the research objectives of this Master's project is to investigate whether it is possible to capture the BOLD signal through the anatomical connectivity map provided by DW-MRI technique. The BOLD activity here is inferred via the Balloon-Windkessel hemodynamic model [6] (Section 2.6). The input of this model is the simulated neuronal activity (Section 2.5), and the output is designed to be a hemodynamic oscillation (< 0.1 Hz) analogous to the BOLD signal (Section 2.6) [6]. The previous section already demonstrated the FitzHugh-Nagumo network model results for the temporal dynamics of brain nodes at the resting-state [5, 11], and this section feeds the extracted time-series into the BOLD activity model.

The extracted time-series for the neuronal activity are chosen from right-hand sides of Figure 3.3 and Figure 3.5, corresponding to the FHN network model simulations of functional and anatomical brain networks in the respective (c, r) and (c, p) parameter spaces. All time-series are normalized around their mean values and then embedded to the hemodynamic model. The comparison of simulated BOLD activity to the empirical fMRI-BOLD data is quantified statistically with the same methodological order as in Section 3.1: *i*) the correlations $\rho_{i,j}$ of the simulated BOLD oscillations of any node pairs i, j among $N = 90$ nodes are calculated via Pearson's coefficients, *ii*) a simulated correlation matrix (CM) of size 90×90 is constructed with all ρ_{ij} values, *iii*) the simulated CM is compared to the empirical functional correlation matrix (FCM) derived from fMRI-BOLD measurement via Pearson's statistical approach again.

Figure 3.9 illustrates statistical comparisons between simulated CM's and the experimental FCM of the BOLD activity. The input of the modeled BOLD activity is the neuronal time-series extracted from functional (Figure 3.9, left) and anatomical (Figure 3.9, right) brain networks (Sections 2.1 and 2.2). The colorbars represent Pearson correlation coefficients $\rho_{e,s}$ between empirical e and simulated s correlation matrices.

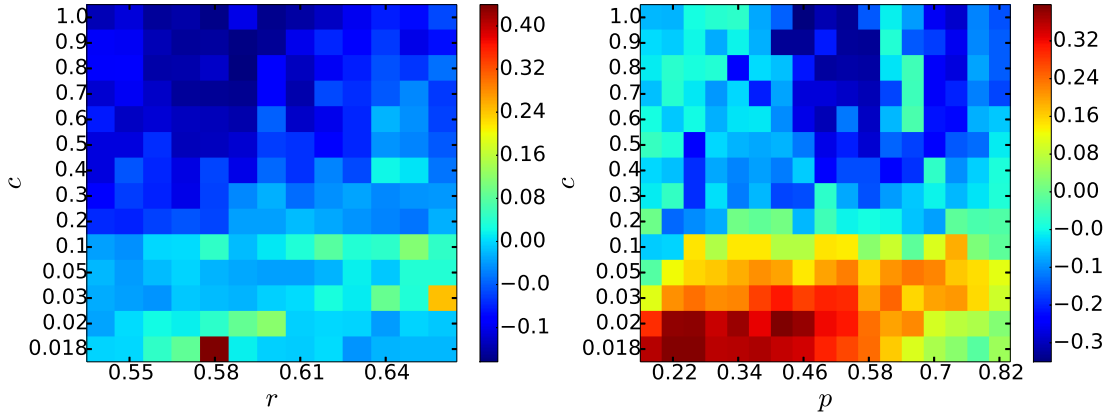


FIGURE 3.9: Parameter analysis for the comparison of fMRI-BOLD data to the modeled BOLD activity on the functional (constant signal propagation velocity $v = 7$ m/s, left) and on the anatomical brain graphs (constant $v = 3$ m/s, right).

In Figure 3.9, the BOLD activity simulations tend to be in better agreement with the empirical FCM at low coupling strength $c \leq 0.1$ for both anatomical and functional brain networks. It can be inferred that, the smaller scaled the neuronal activity oscillations are, the higher correlation between the BOLD simulations and fMRI-BOLD data is captured. The anatomical brain networks exhibit a finer correlation pattern compared to the functional brain networks. It is possible to capture functional BOLD fluctuations observed in fMRI at the resting-state through the structural connectivity of the brain, especially at low coupling strength c , a low axonal propagation velocity $v = 3$ m/s and $p < 0.70$ (hot colors in Figure 3.9, right).

The network topology of anatomical brain graphs has a more pronounced effect for the $\rho_{e,s}$ values in comparison to that of functional brain graph. $0.18 < p < 0.70$ corresponds to very smoothly changing network measurements in the brain graphs obtained from DW-MRI data (Section 2.4, Appendix B). Figure 3.9 (left) does not have a well-interpreted $\rho_{e,s}$ -pattern in the (r, c) parameter space. $0.54 < r < 0.66$ corresponds to sharply changing network properties in the functional brain graphs. The $\rho_{e,s}$ -values in Figure 3.9 (left) are mostly around zero or weak correlation.

Figures 3.10 demonstrates the simulated CM of BOLD activity extracted from functional brain graph together with the empirical (FCM) obtained from fMRI-BOLD technique. The simulated CM is chosen from green/orange-colored parameters in Figure 3.9 (left). The Pearson correlation coefficient between the simulated CM and the empirical FCM

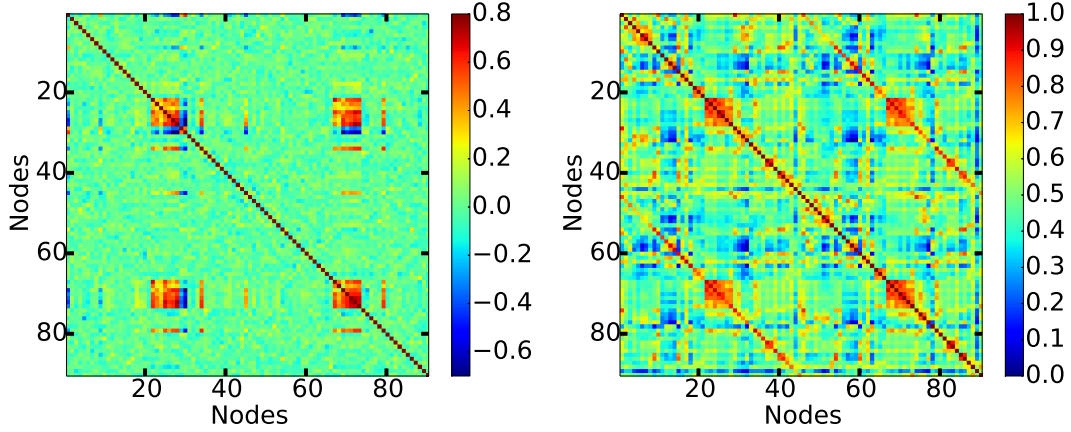


FIGURE 3.10: Correlated BOLD activity simulation of functional brain graph with $c = 0.03$, $v = 7$ m/s and $r = 0.66$ (left) and empirical FCM derived from fMRI-BOLD technique, $\rho_{e,s} = 0.24$.

is $\rho_{e,s} = 0.24$. This is a relatively low correlation coefficient compared to the $\rho_{e,s}$ -values captured for the simulated neuronal activity in Section 3.1.

In Figure 3.10, the trace of subdiagonals in the empirical FCM is lost in the simulated CM. However, both matrices have common neuronal populations (or brain nodes) in the left and right hemispheres, whose correlated BOLD activity tend to be almost equivalently strong, see hot colored subsquares in simulated CM and FCM.

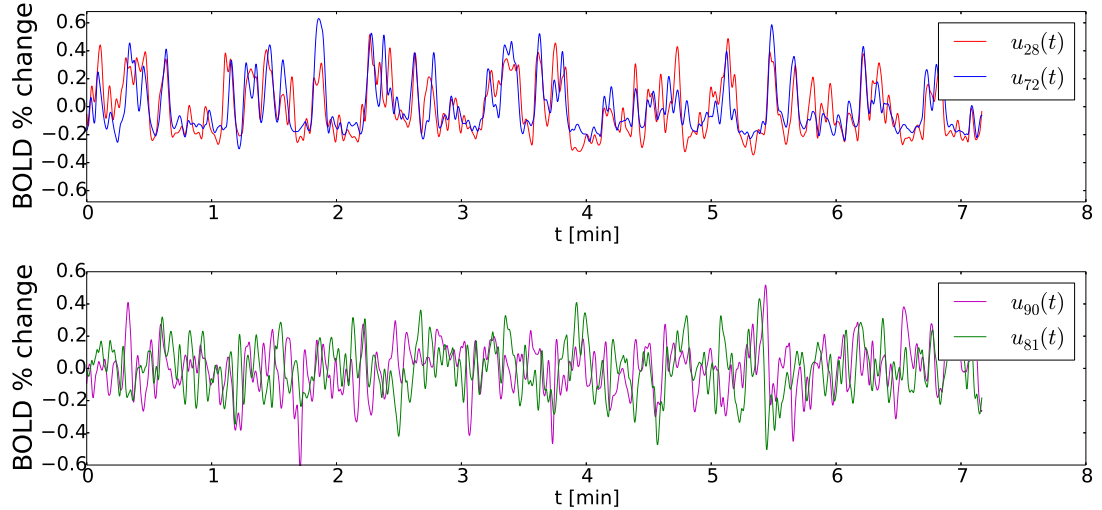


FIGURE 3.11: Simulated BOLD activity of highly (top, $\rho_{28,72} = 0.75$) and poorly (bottom, $\rho_{90,81} = 0.10$) correlated node couples. Both nodes are chosen from the simulated CM in Figure 3.10 ($c = 0.03$, $v = 7$ m/s, $r = 0.66$).

Figure 3.11 illustrates temporal dynamics of the simulated BOLD activity of two node pairs. The extracted BOLD oscillations of nodes 28 and 72 are synchronized, $\rho_{28,72} =$

0.75. The BOLD fluctuation of nodes 90 and 81 are poorly correlated, $\rho_{90,81} = 0.10$. These node couples are chosen from hot and cold color parameters in Figure 3.10 (left).

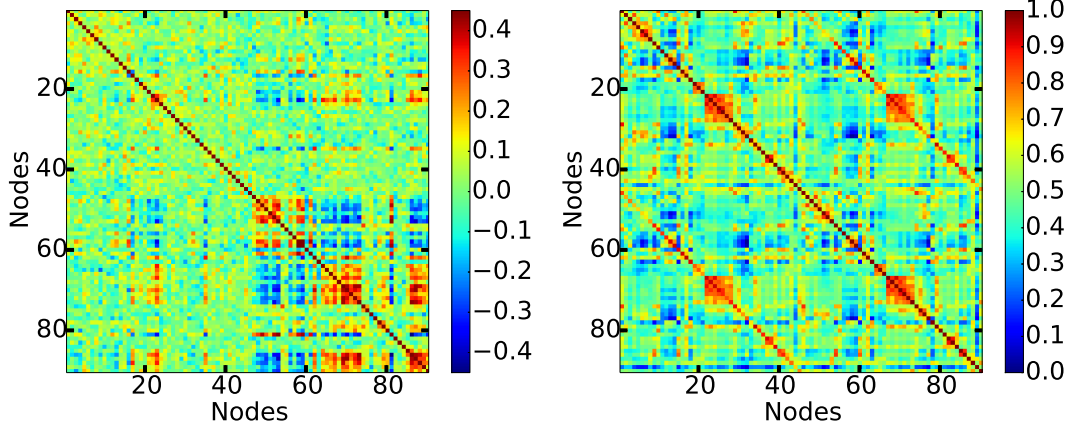


FIGURE 3.12: Correlated BOLD activity simulation of anatomical brain graph with $c = 0.03$, $v = 3$ m/s and $p = 0.54$ (left) and empirical FCM derived from fMRI-BOLD technique, $\rho_{e,s} = 0.22$.

Figures 3.12 illustrates the simulated CM of BOLD activity extracted from anatomical brain graph (left) together with the empirical (FCM) obtained from fMRI-BOLD measurement (right). The simulated CM is chosen from red/orange-colored parameters in Figure 3.9 (right). The Pearson correlation coefficient between the simulated CM and the empirical FCM is $\rho_{e,s} = 0.22$. This is again a relatively low correlation coefficient compared to Section 3.1.

In Figure 3.12, the trace of subdiagonals in the empirical FCM is almost lost in the simulated CM. The nodes in right and left hemispheres correlate around $\rho_{i,j} = 0.1$ in the simulated CM (yellowish subdiagonals on CM), while they are highly correlated empirically (red subdiagonals in FCM). The correlations between node pairs located in left-left, right-right, left-right and right-left can be distinguished in both CM and FCM. Both matrices have distinct neuronal populations (or brain nodes), whose correlated BOLD activity tend to be high, see hot-colored subsquares in Figure 3.12. However, these subpopulations do not refer exactly to the same AAL regions in CM and in FCM, but they are at least on the same hemisphere.

Figure 3.13 demonstrates temporal dynamics of the simulated BOLD activity of two node pairs chosen from anatomical brain graph. The extracted BOLD oscillations of nodes 58 and 59 are synchronized, $\rho_{58,59} = 0.48$. The BOLD fluctuation of nodes 90

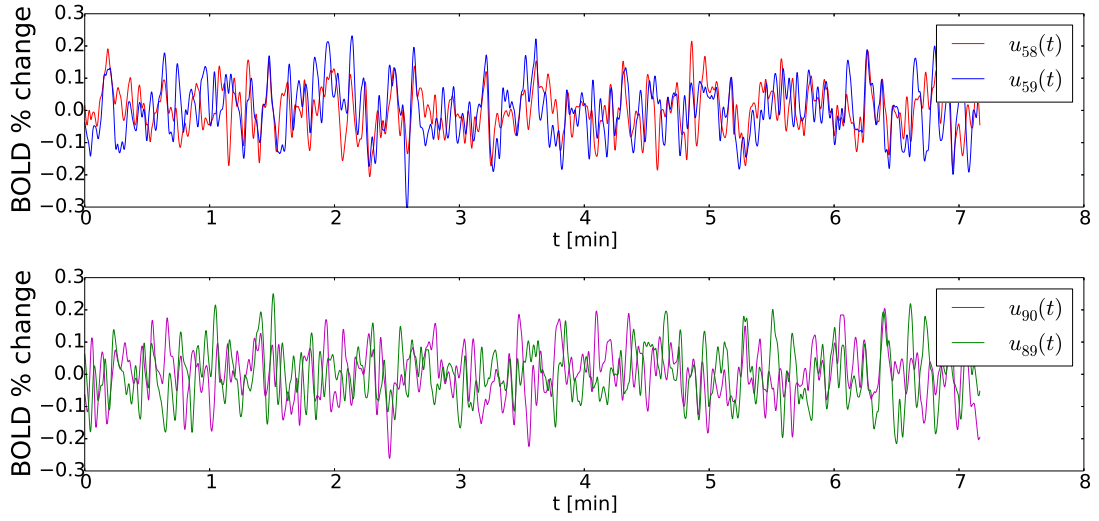


FIGURE 3.13: Simulated BOLD activity of highly (top, $\rho_{58,59} = 0.48$) and poorly (bottom, $\rho_{90,89} = 0.11$) correlated node couples. Both nodes are chosen from the simulated CM in Figure 3.12 ($c = 0.03$, $v = 3$ m/s, $p = 0.54$).

and 89 are poorly correlated, $\rho_{90,89} = 0.11$. These node couples are chosen from hot and cold color parameters from the simulated CM in Figure 3.12 (left).

This subsection closes with a fast Fourier transform analysis performed for the oscillation frequencies ν of simulated BOLD activity model on functional and brain graphs. The simulated CM's visualized in Figure 3.10 and 3.12 are chosen as exemplary simulated brain connectivity maps at the resting-state. Figure 3.14 visualizes the pronounced ν -ranges identified for all $N = 90$ nodes in functional (top) and anatomical brain graphs (bottom). The power spectrum indicates that, BOLD fluctuations are dominant around $\nu = 0.1$ Hz and they are uniform over all nodes. The ν -range on the x -axis is limited to 2 Hz, since there is no higher ν than 2 Hz is observed for the BOLD activity simulations.

Given a fast oscillating neuronal time-series as the input, the Balloon-Windkessel hemodynamic model [6] acts on it as a low-pass filter. The resulting fluctuations are ultra slow in the frequency range. This section showed that the modeled hemodynamic model resulted in plausible BOLD oscillations around 0.1 Hz. It is possible to capture the traces of BOLD fluctuations by modeling the structural connectivity map of the brain (Figure 3.9, left). However, the simulated CM's of BOLD activity are not yet fully in agreement with the empirical FCM (Figure 3.9, 3.10 and 3.12). The Ballon-Windkessel model in Friston et al. was not designed for the resting-state dynamics of the brain [6].

The hemodynamic model can be further investigated with a better resting-state adaptations, i.e. its standard parameters could be recovered for the resting-state. Another approach would be analyzing the low coupled ($c \leq 0.1$) FitzHugh-Nagumo oscillators in a broader manner to provide more plausible time-series input to the BOLD model.

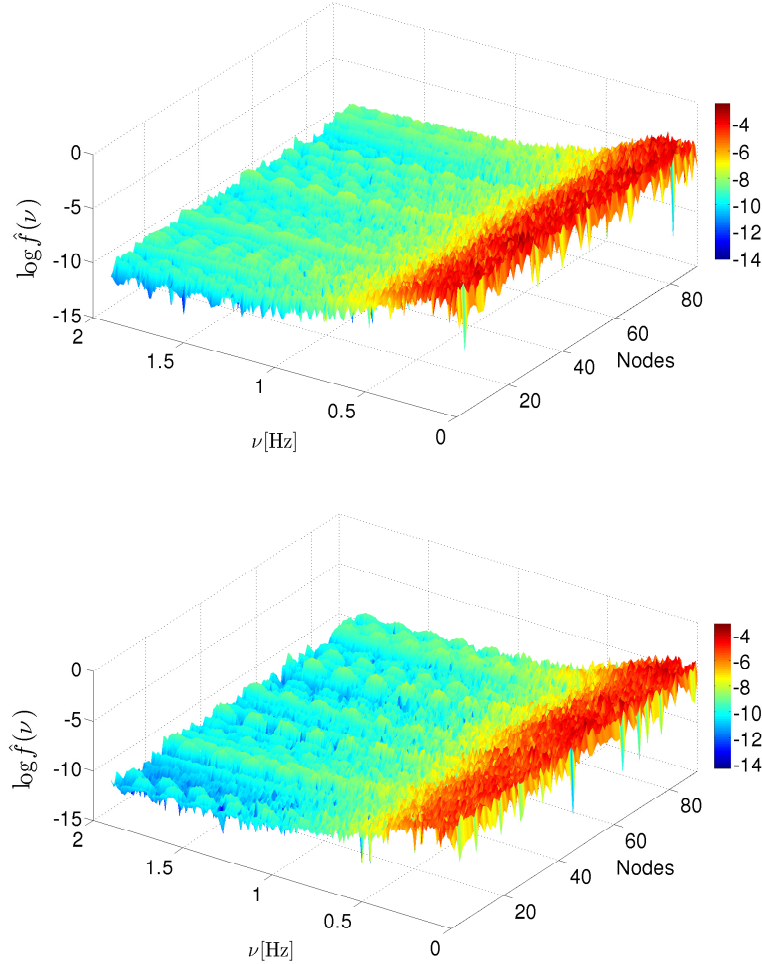


FIGURE 3.14: Illustration of fast Fourier transform of simulated BOLD activity oscillations corresponding to $N = 90$ nodes in functional (top) and anatomical (bottom) brain graphs.

3.3 Comparison of Brain Graphs to Random Graphs

This section implements methods drawn from graph theory/network science in order to investigate the spatial and temporal dynamics of human brain at resting-state. The brain graphs R_{BG} are constructed on the functional and anatomical connectivity maps derived from fMRI-BOLD and DW-MRI measurements, respectively (Section 2.1 and 2.2). The

spatial dynamics of each network is identified in dependence on the threshold level r for the functional connectivity (FC) and on the probability level p for the anatomical connectivity (AC) maps of the brain. In particular, I aim to explore such conditions that distinguish the modeled neuronal activity of brain graphs from that of random networks. The random graphs are built with five randomization procedures: Erdős-Rényi R_{ER} , double-edge-swap R_{DES} , preserved-degree-distribution R_{PDD} , configuration model R_{CM} and partial randomization R_{PR} methods (Section 2.3, Table 2.1).

The neuronal activity of $N = 90$ AAL nodes in each network is modeled via FitzHugh-Nagumo (FHN) oscillators [5, 11] (Section 2.5). The Pearson correlation coefficients ρ between any pairwise combinations of $N = 90$ nodes are calculated for the extracted neuronal time-series. These correlation coefficients are then distributed in histogram for each network at the corresponding r or p values and FHN parameters.

Figure 3.15 demonstrates an exemplary couple of histograms. The correlations between all possible pairwise correlations among $N = 90$ time-series is $0 \leq \rho \leq 1$ on the x -axis. The number of paired nodes, whose correlations fell into a defined ρ -range, is normalized on the y -axis. FC map related R_{BG} histogram (Figure 3.15, left) resembles a uniform distribution around 0, meaning dominant no-correlations among neural time-series. AC map related R_{BG} histogram (Figure 3.15, right) has more frequently correlated time-series observed with ρ -values close to 1.0.

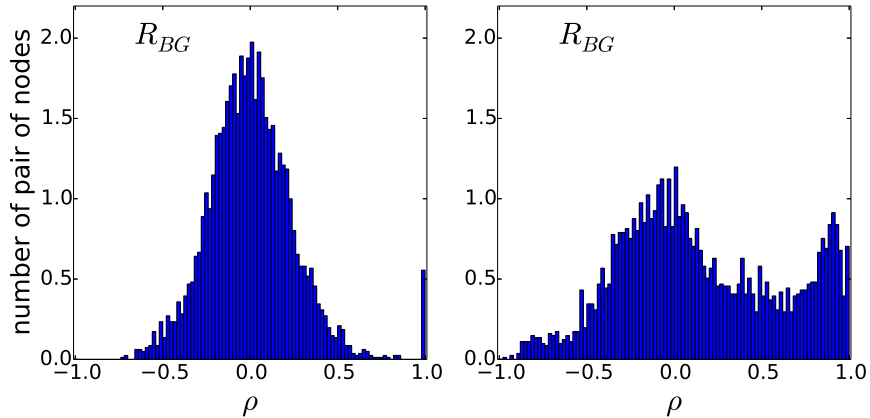


FIGURE 3.15: Histograms for the distribution of Pearson correlation coefficients ρ among all possible pairwise combinations of nodes. On the left: R_{BG} obtained from FC map at $r = 0.61$, FHN model parameters $c = 0.1$, $v = 7$ m/s. On the right: R_{BG} obtained from AC map at $p = 0.42$, FHN model parameters $c = 0.5$, $v = 6$ m/s.

Investigating the analogy between random and brain graphs requires another statistical approach than Pearson's analysis, since both graph types are not identical in terms of their network topology. The degree of similarity between brain graphs and random networks is quantified with Bhattacharya coefficients, a widely used statistical approach to measure the correlation between statistical samples, i.e. histograms [50]. Let us denote the ρ distributions of simulated neuronal activity of a brain graph with H_b and that of random graph with H_r , the Bhattacharya coefficient $d(H_b, H_r)$ is given by the following equation:

$$d(H_b, H_r) = \sqrt{1 - \frac{1}{\sqrt{\bar{H}_r \bar{H}_b N^2}} \sum_i \sqrt{H_r(i) H_b(i)}}, \quad (3.2)$$

where \bar{H} denotes the mean of histogram [50]. $d(H_b, H_r)$ is scaled between 0 and 1. A high $d(H_b, H_r)$ value indicates a low correlation between H_b and H_r , whereas a low $d(H_b, H_r)$ value expresses a high degree of similarity.

Brain graphs derived from *i*) FC map and *ii*) AC map are compared to the random networks separately as demonstrated in the next two subsections. Bhattacharya coefficients are used to quantify the analogy between brain and random graphs. The purpose is to investigate high $d(H_b, H_r)$ values indicating a diversity between brain and random graphs in the (r, c) parameter spaces, where c is the coupling strength for the functionally interacting nodes (Section 2.5).

3.3.1 Comparing Functional Brain Graph to the Random Graphs

The fMRI-BOLD functional connectivity (FC) map is binarized via thresholding at $0.54 \leq r \leq 0.66$ range by step size of 0.01. An adjacency matrix (AM) is obtained for each r -value, indicating functionally connected node pairs with 1's and unconnected pairs with 0's (Section 2.2). AM's are used as the principal matrix structure to construct the brain graphs R_{BG} with NETWORKX tool (Section 2.2). The random networks R_{ER} , R_{DES} , R_{PDD} , R_{CM} , R_{PR} are generated by manipulating the topology of R_{BG} with randomization procedures described in Section 2.3. The topological network measures of R_{BG} and all random networks are characterized in Section 2.3 and Appendix B.

The random graphs and the brain graph R_{BG} are simulated with the FHN network model (Section 2.5). The correlations ρ among the time-series of node pairs are calculated via Pearson coefficients and distributed in histograms.

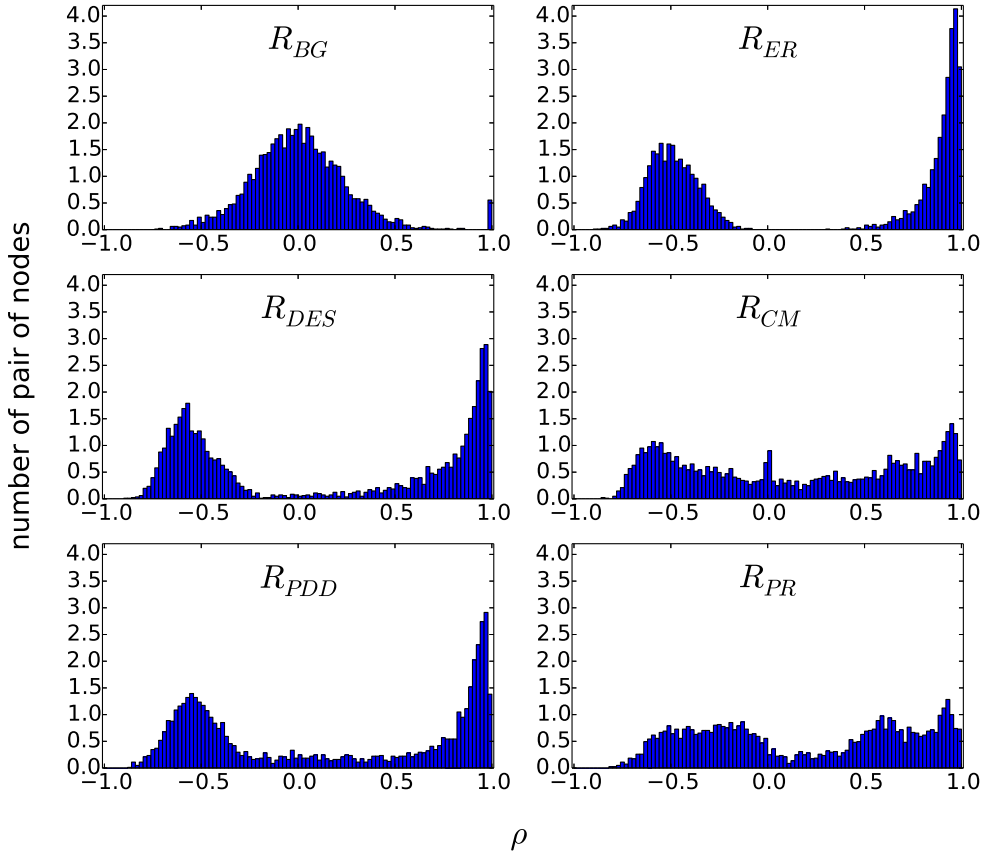


FIGURE 3.16: Histograms for the distributions of ρ among all pairwise combinations of nodal time-series in FC map related graphs (left column, from top to bottom: R_{BG} , R_{DES} , R_{PDD} , right column, from top to bottom: R_{ER} , R_{CM} , R_{PR}). The FHN network model parameters for the chosen graphs are $c = 0.1$, $v = 7$ m/s, network topology parameter $r = 0.61$.

Figure 3.16 demonstrates an exemplary set of histogram distributions of ρ -values for the neuronal time-series extracted from R_{BG} as well as five random networks. The distribution of ρ values of the time-series in the R_{BG} resembles a normal distribution around mean 0, indicating that the nodes are mostly not correlated in terms of their modeled neuronal activity. The unique peak around $\rho = 1.0$ represents the self combination of nodes, i.e. $\rho_{i,i} = 1.0$ for any node i as expected. The ρ values in R_{ER} , R_{DES} and R_{PDD} are observed more frequently at $\rho \approx -0.5$ and $0.5 < \rho \leq 1.0$, indicating anti-correlated

and correlated FHN modeled time-series. However, R_{CM} and P_{PR} graphs tend to have more smoothly distributed ρ -values between anti-correlation and high correlation.

Histogram distribution of ρ values between all possible node pairs in a graph is further used to compare FHN network model simulations of R_{BG} to that of the random networks. This comparison is quantified with the Bhattacharya coefficient and carried in (r, c) parameter space. r will yield us to interpret the spatial dynamics of the networks, whereas the coupling strength c will be used to understand the temporal dynamics of modeled neuronal activity. The previous section 3.1.1 has already demonstrated the effect of c and the axonal signal propagation v parameters of the FHN network model in detail. Here, v is fixed to 7 m/s, at which the temporal dynamics of R_{BG} resulted in high agreement with the empirical fMRI-BOLD data (Section 3.1.1).

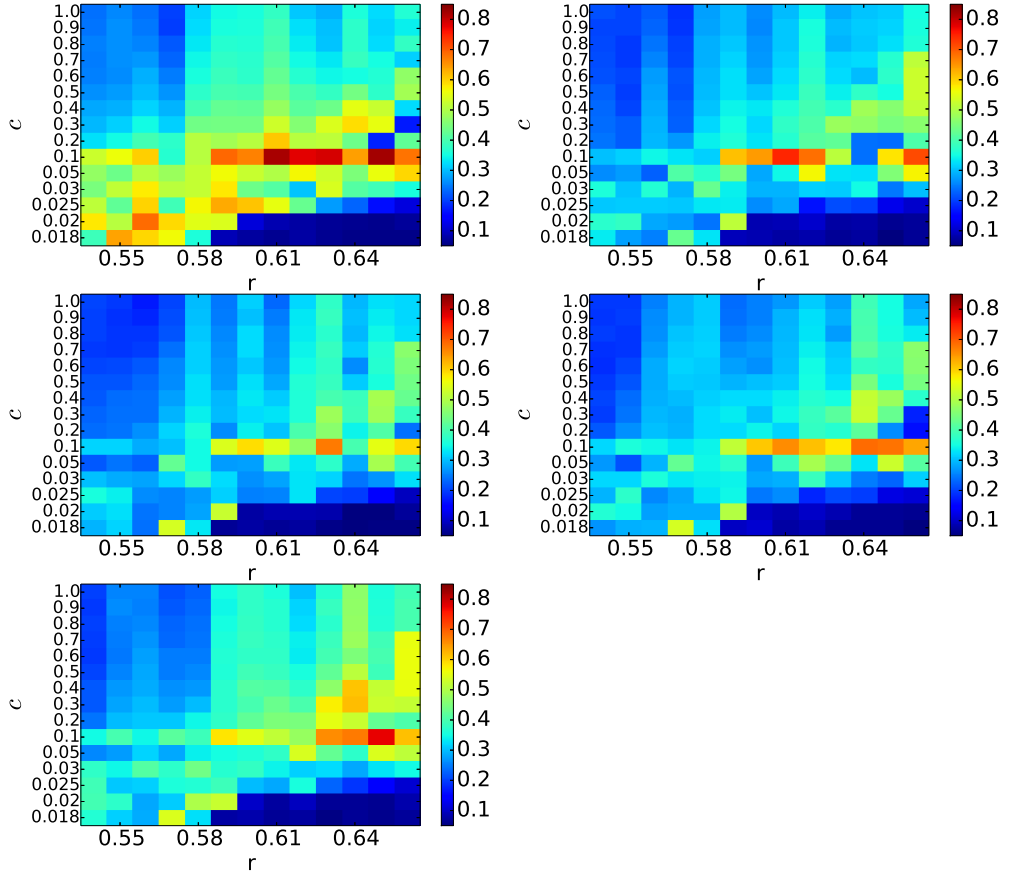


FIGURE 3.17: Each heat map corresponds to statistical comparison of brain graph to random graphs in terms of FHN network modeled time-series (left column, from top to bottom: $d(H_{BG}, H_{ER})$, $d(H_{BG}, H_{CM})$, $d(H_{BG}, H_{PR})$, right column, from top to bottom: $d(H_{BG}, H_{DES})$, $d(H_{BG}, H_{PDD})$).

Figure 3.17 represents the Bhattacharya coefficients $d(H_b, H_r)$ between the FC related brain graph and five types of random networks, i.e. $d(H_{BG}, H_{ER})$, $d(H_{BG}, H_{CM})$, $d(H_{BG}, H_{PR})$ $d(H_{BG}, H_{DES})$, $d(H_{BG}, H_{PDD})$. The colorbars express the magnitude of $d(H_b, H_r)$. The hot colors indicate a diversity between R_{BG} and the random graph, whereas the cold colors denote an analogy.

The FHN network modeled temporal dynamics of nodes in R_{BG} tends to be different than random graphs generally at high r - and intermediate c -values, as it is quantified with Bhattacharya coefficients in Figure 3.17. The network density κ of all the FC map related networks fell below 0.18 for $r > 0.60$ (Section 2.4.1). These less dense networks become explicitly different in terms of their network topology (Section 2.4, Appendix B). The intermediate c -values, particularly $c = 0.1$, make the temporal dynamics of R_{BG} distinct from that of random graphs.

Among all random graphs, R_{BG} is the most frequently distinguishable than Erdős-Rényi-type network R_{ER} in (r, c) parameter space. This diversity is observed well pronounced at two parameter space regions: low r - low c and high r - intermediate c regions. The network topology of R_{BG} and R_{ER} is only slightly different at $r < 0.6$ (Section 2.4, Appendix B). However, small scaled oscillations of the FHN network modeled nodes at $c < 0.1$ bring distinct temporal dynamics to R_{BG} and R_{ER} . At $r > 0.6$, where the network topology measures explicitly differ for both R_{BG} and R_{ER} , the simulated temporal dynamics of R_{BG} varies from that of R_{ER} at only intermediate values of c .

Finally, it has been explored that, the modeled temporal dynamics of R_{BG} obtained from FC map can be distinguished from that of random networks at parameter space (r, c) . The next subsection will compare the R_{BG} derived from AC map to the random networks in the same methodological order.

3.3.2 Comparing Anatomical Brain Graph to the Random Graphs

The DW-MRI anatomical connectivity (AC) map is binarized via probability values in $0.38 \leq p \leq 0.82$ range by amount of 0.04 step size. An adjacency matrix (AM) is obtained for each p value, indicating structurally connected node pairs with 1's and unconnected pairs with 0's at given anatomical connection probability p (Section 2.2). As explained in the previous subsection, AM's are used to build the brain graphs R_{BG} . The

random networks R_{ER} , R_{DES} , R_{PDD} , R_{CM} , R_{PR} are generated with the randomization tools by manipulating the network topology of R_{BG} (Section 2.3).

The methodological order to compare R_{BG} to the random networks is the same as in the previous subsection: *i*) all graph types are simulated with the FHN network model, *ii*) the time-series of each pair of nodes are compared by Pearson's correlation coefficient ρ , *iii*) the histogram distribution of ρ values are obtained for each graph type and finally all the histograms are compared with Bhattacharya coefficients.

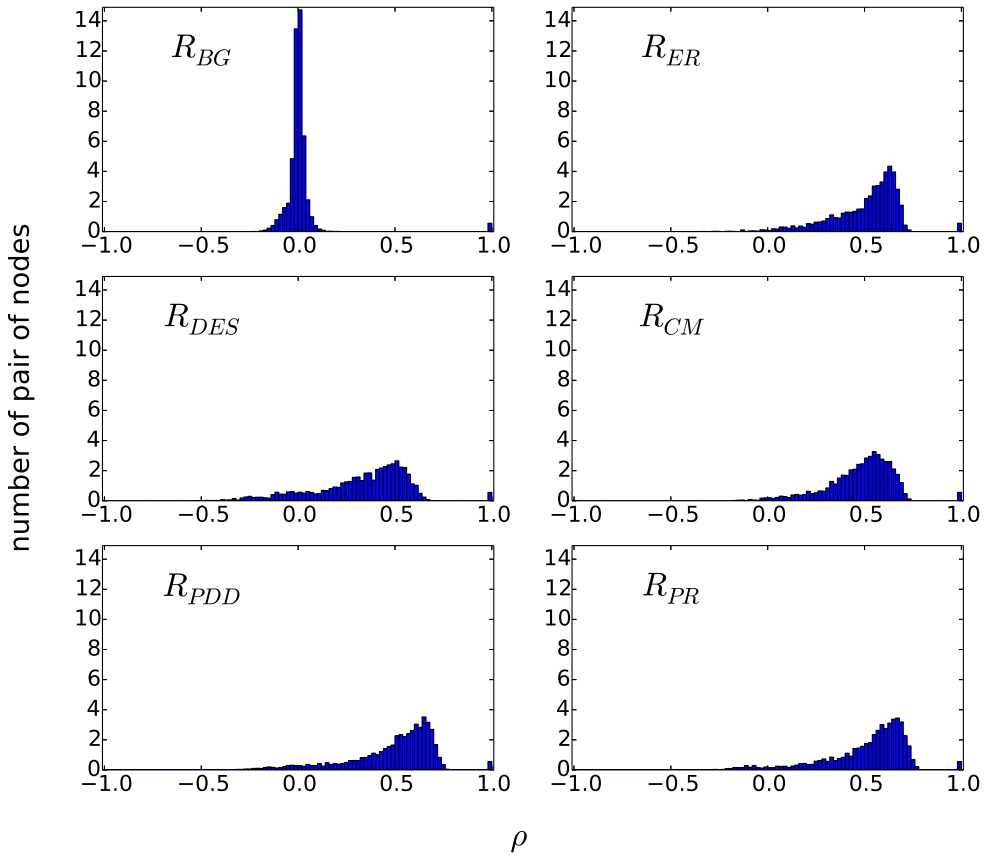


FIGURE 3.18: Histograms for the distributions of ρ among all pairwise combinations of nodal time-series in AC map related graphs (left column, from top to bottom: R_{BG} , R_{DES} , R_{PDD} , right column, from top to bottom: R_{ER} , R_{CM} , R_{PR}). The FHN network model parameters for the chosen graphs are $c = 0.02$, $v = 6$ m/s, network topology parameter $p = 0.58$.

Figure 3.18 illustrates an exemplary set of histograms of ρ values for the R_{BG} , which is constructed on an AM obtained at $p = 0.58$ and five random graphs, which are built by manipulating this AM via randomization tools provided by NETWORX and BCT

algorithms (Section 2.3) [30, 33]. The parameters of the neuronal time-series are the coupling strength $c = 0.02$ and the signal propagation velocity along axons $v = 6$ m/s.

The frequency of ρ values in R_{BG} resembles a normal distribution around mean 0, indicating the dominance of non-correlated node pairs in terms of their modeled temporal dynamics. All random networks tend to have correlated time-series around $\rho = 0.5$ the most frequently, and they exhibit almost no anti-correlation. The peaks at $\rho = 1.0$ in each graph corresponds to self-paired nodes, i.e. $\rho_{i,i} = 1.0$ for node i .

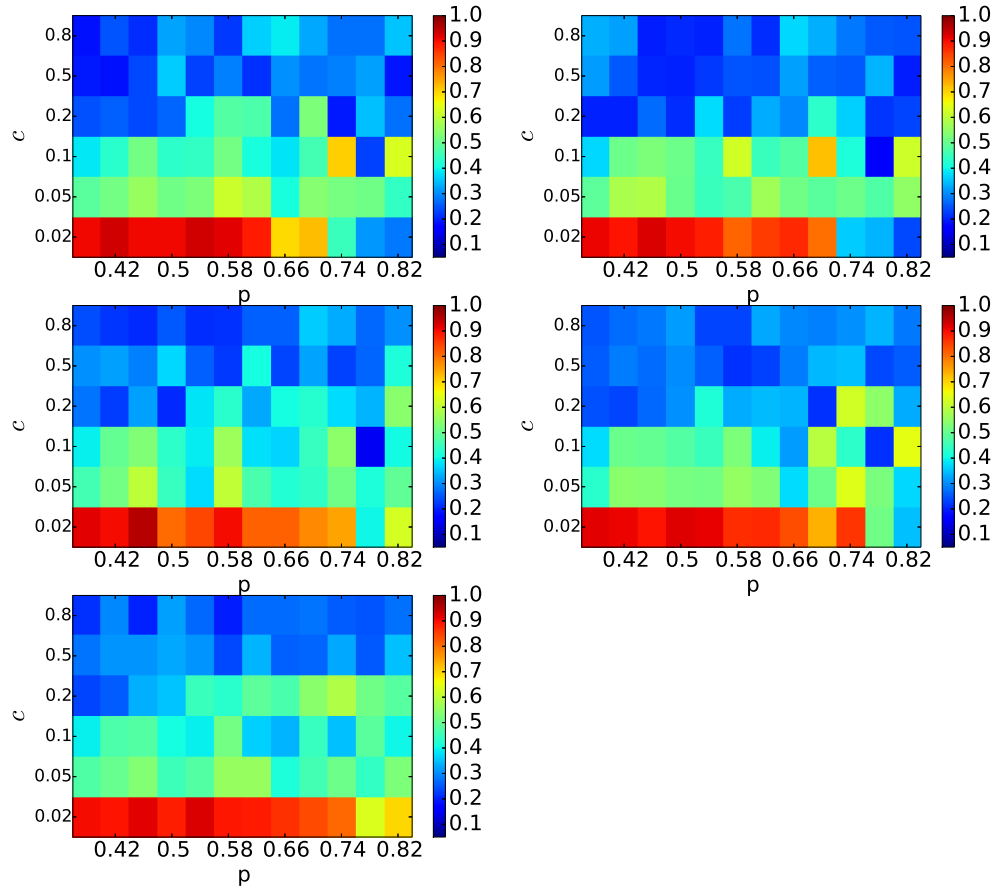


FIGURE 3.19: Each heat map corresponds to statistical comparison of brain graph to random graphs in terms of FHN network modeled time-series (left column, from top to bottom: $d(H_{BG}, H_{ER})$, $d(H_{BG}, H_{CM})$, $d(H_{BG}, H_{PR})$, right column, from top to bottom: $d(H_{BG}, H_{DES})$, $d(H_{BG}, H_{PDD})$).

Figure 3.19 represents the Bhattacharya coefficients $d(H_b, H_r)$ between the AC related brain graph and five types of random networks, i.e. $d(H_{BG}, H_{ER})$, $d(H_{BG}, H_{CM})$, $d(H_{BG}, H_{PR})$, $d(H_{BG}, H_{DES})$, $d(H_{BG}, H_{PDD})$. The colorbars express the magnitude of $d(H_b, H_r)$. The hot colors indicate a diversity between R_{BG} and the random graph, whereas the cold colors denote an analogy.

The anatomical connectivity map related brain graph R_{BG} and its randomized networks are clearly distinguishable at $0.38 \leq p \leq 0.7$ and at low c -values 0.1, 0.05, 0.02. The p -range corresponds to a network density of $0.18 \geq \kappa \geq 0.15$ for all AC related graphs (Section 2.4.1). The network topology of random networks R_{ER} , R_{DES} , R_{PDD} , R_{CM} , R_{PR} are quite similar to each other in this κ -range (Section 2.4, Appendix B). However, the network properties of R_{BG} are distinct from random networks. This diversity can be preserved in terms of temporal dynamics of network types at low coupling strength c , meaning small scaled FHN oscillations.

At $1 \geq p > 0.7$, the topology of R_{BG} begin to change dramatically, shortest pathway d_{ij} and small worldness S increases suddenly, global and local efficiency drops to zero (Appendix B). In terms of modeled temporal brain dynamics, R_{BG} above $p > 0.7$ becomes less different than random graphs, especially at large scale oscillating brain nodes at $c > 0.1$.

This section demonstrated that the FHN network model on anatomical brain graph makes it possible to distinguish the neuronal time-series of R_{BG} from that of random networks. This proposal was also captured for the functional brain graphs in the previous section.

Chapter 4

Conclusion and Discussion

The project utilizes modeling approaches combined with empirical results to resolve underlying biophysical mechanisms of human brain at resting state. Empirical brain connectivity maps of resting state are obtained from fMRI-BOLD and DW-MRI techniques, revealing functional and anatomical connections among AAL regions, respectively. The modeling approaches are implemented to discover *i*) neuronal activity time-series, *ii*) ultra-slow BOLD fluctuations, and *iii*) to investigate topological properties of brain graphs. Temporal dynamics of neuronal populations is built on FitzHugh-Nagumo (FHN) oscillations [5, 10, 12, 37]. The BOLD activity is inferred via the Balloon-Windkessel hemodynamic model, which takes the normalized FHN time-series as an input [5, 6]. The spatial properties of brain graphs are discussed by comparing network measures of brain graphs to randomly constructed graphs with statistical methods [8, 15, 17]. The research proposal is capture temporal fMRI-BOLD dynamics through structural connectivity map of brain, while discussing if the spatial topology properties of brain networks are distinguishable than that of random graphs.

The fMRI-BOLD functional correlation matrix can be recaptured with FHN modeled neuronal activity dynamics at high axonal signal propagation velocity $v > 6$ m/s, at intermediate coupling strength $0.1 < c < 0.4$ and at threshold $0.54 < r < 0.60$. These parameter ranges are in agreement with previous studies [5, 11]. It is possible to follow traces of highly correlating AAL regions located symmetrically on right and left hemispheres as presented with sub-diagonals in Figure 3.2, left.

The DW-MRI anatomical correlation matrix can also be imitated with FHN model applied on ACM based brain graphs at $v > 4$ m/s, at $0.1 < c < 0.5$, and at connection probability range $0.18 < p < 0.70$. The symmetry of empirical correlation matrix is preserved in simulated correlation matrix as seen in Figure 3.6.

Brain graphs are constructed on adjacency matrices, which are binarized empirical FCMs and ACMs via r and p , respectively. Here, r - and p -values yield us to identify network topology of simulated brain graphs, i.e. $0.54 < r < 0.60$ corresponds to a network density $0.50 < \kappa_{FCM} < 0.18$ for FCM graphs, and $0.18 < p < 0.70$ that of $0.30 < \kappa_{ACM} < 0.18$ for ACM graphs. The lower boundaries present the limit of PYDELAY module for the numerical solution of time-delayed differential equations of FHN model. The upper limits are restrained with statistical characterizations of brain graphs. Beyond $\kappa_{FCM} < 0.18$ and $\kappa_{ACM} < 0.18$, less densely connected brain networks exhibit dramatically changing transitivity T , shortest pathway d_{ij} , small worldness S and assortativity A , and simulations become distinctly different from experiment (See Section 2.4 and Appendix B).

One of the key proposals of this master's thesis is to investigate whether it is possible to catch BOLD fluctuations through structural connections in the human brain at resting state. FHN neuronal activity model is promising, but it is not a complete approach for BOLD dynamics due to high frequency oscillations $20 \text{ Hz} < \nu < 60 \text{ Hz}$ of type-II excitable neuronal populations. The inferred Balloon-Windkessel model provides high correlations between FCM based BOLD simulations and fMRI-BOLD data at $c < 0.1$, stating that inferred BOLD activity model is plausible at least for the less strongly functionally coupled neurons. However, the principal step is to capture BOLD fluctuations via ACM brain graphs for the thesis proposal. The correlation between ACM based BOLD simulations and fMRI-BOLD is found to be restricted by a Pearson correlation coefficient of $\rho_{e,s} = 0.22$ on parameter space (p, c) (Figure 3.9 and 3.12). The coupling strength range is $c < 0.1$ for high correlations. Oppositely to FHN neuronal activity simulations, the BOLD fluctuations become more reasonable at very small c for ACM and FCM graphs. c scales the amplitude of neuronal activity oscillations, so, small scaled FHN oscillating neurons turn out better BOLD activity simulations. The parameter analysis of simulated activity of BOLD signal for ACM graphs can be designed with finer c values with this deduction in future.

The intrinsic properties of a brain network have a significant effect on its temporal dynamics. This proposal is evidenced statistically, when the modeled neuronal activities of nodes in the brain graph is compared to that of random graphs. The brain graphs are found to be distinguishable than random graphs at specific parameter ranges, i.e. at low coupling strength, in terms of extracted FHN time-series.

Appendix A

Automated Anatomical Labeling

The human brain is segmented into $N = 90$ cortical and sub-cortical regions according to the Tzourio-Mazoyer brain atlas with the automated anatomical labeling (AAL) template [4], such that regions with index $n = \{1, 2, \dots, 45\}$ lie on the right hemisphere, whereas $n = \{46, 47, \dots, 90\}$ are on the left. The fMRI-BOLD activity is measured from all voxels in an AAL region. FCM reveals the correlation of measured BOLD signal between pairwise combinations of AAL regions. The anatomical connectivity matrix (ACM) used in this project is obtained from the study of Iturria-Medina et al. [28] and it is based on the same $N = 90$ AAL regions as in the FCM. Each value in ACM reveals the probability of any 2 AAL regions being connected via axonal fibers. Table A.1 describes AAL regions.

TABLE A.1: Anatomical Description of Brain Nodes

Index R/L	Anatomical Description	Label
1/46	Precentral	PRE
2/47	Frontal Sup	F1
3/48	Frontal Sup Orb	F10
4/49	Frontal Mid	F2
5/50	Frontal Mid Orb	F20
6/51	Frontal Inf Oper	F30P
7/52	Frontal Inf Tri	F3T
8/53	Frontal Inf Orb	F30
9/54	Rolandic Oper	RO
10/55	Supp Motor Area	SMA
11/56	Olfactory	OC
12/57	Frontal Sup Medial	F1M
13/58	Frontal Mid Orb	SMG
14/59	Gyrus Rectus	GR
15/60	Insula	IN
16/61	Cingulum Ant	ACIN
17/62	Cingulum Mid	MCIN
18/63	Cingulum Post	PCIN
19/64	Hippocampus	HIP
20/65	ParaHippocampal	PHIP
21/66	Amygdala	AMYG
22/67	Calcarine	V1
23/68	Cuneus	Q
24/69	Lingual	LING
25/70	Occipital Sup	O1
26/71	Occipital Mid	O2
27/72	Occipital Inf	O3
28/73	Fusiform	FUSI
29/74	Postcentral	POST
30/75	Parietal Sup	P1
31/76	Parietal Inf	P2
32/77	Supra Marginal Gyrus	SMG
33/78	Angular	AG
34/79	Precuneus	PQ
35/80	Paracentral Lobule	PCL
36/81	Caudate	CAM
37/82	Putamen	PUT
38/83	Pallidum	PAL
39/84	Thalamus	THA
40/85	Heschi	HES
41/86	Temporal Sup	T1
42/87	Temporal Pole sup	T1P
43/88	Temporal Mid	T2
44/89	Temporal Pole Mid	T2P
45/90	Temporal Inf	T3

Appendix B

Network Characterizations

B.1 Average Degree

Degree k_i is the number of edges connected to the node i . Average degree of a network $\langle k \rangle$ indicates the ratio of total number of edges, L , to total number of nodes, N in a graph,

$$\langle k \rangle = \frac{2L}{N} . \quad (\text{B.1})$$

In order not to count each link twice, the total number of edges is divided by $\frac{N}{2}$ instead of N .

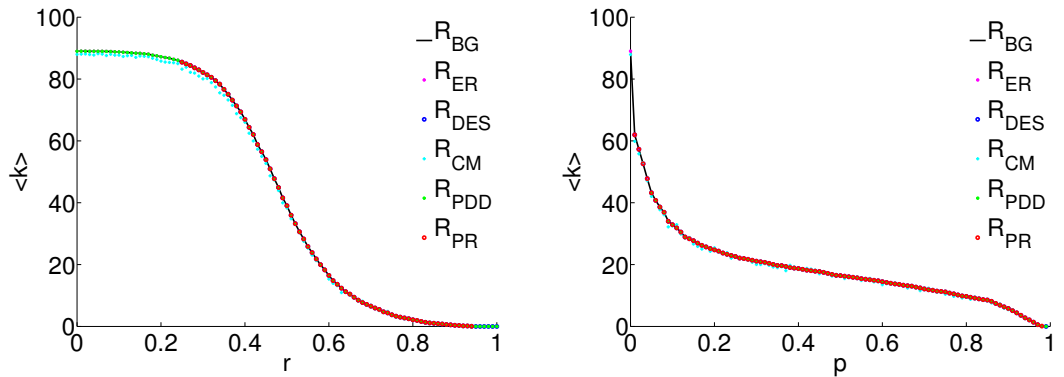


FIGURE B.1: Average degrees of the brain network and the randomized networks, FC map related graphs on the left, AC map related graphs on the right. Successful r ranges for randomization methods of FCM: $r_{ER} = [0, 1]$, $r_{DES} = [0.25, 1.00]$, $r_{CM} = [0, 1.00]$, $r_{PDD} = [0, 1.00]$, $r_{PR} = [0.08, 0.94]$. Successful p ranges of ACM: $p_{ER} = [0, 0.99]$, $p_{DES} = [0.01, 0.99]$, $p_{CM} = [0, 0.99]$, $p_{PDD} = [0.05, 0.98]$, $p_{PR} = [0, 0.99]$.

Degree is one of the statistical tools to measure the centrality of network. The higher the average degree is, the more interaction the nodes in the graph have.

Increasing threshold and probability values diminishes number of edges inverse sigmoidally. As long as the total node numbers, total edge numbers and networks density are all preserved while constructing the random graphs, the average degree remains the same.

B.2 Average Shortest Pathway

Shortest pathway d_{ij} is a measure of integration in the network, opposite to the segregation measures. It corresponds to the shortest path length between two nodes in an unweighted graph,

$$d_{ij} = \sum_{a_{uv} \in g_{i \leftrightarrow j}} a_{uv} , \quad (\text{B.2})$$

where $g_{i \leftrightarrow j}$ is the shortest path between nodes i and j , d_{ij} is assumed to be ∞ for disconnected pairs [20]. (d_{ij} is an integer here, it should not confused with distance matrix given in Appendix C.) The d_{ij}

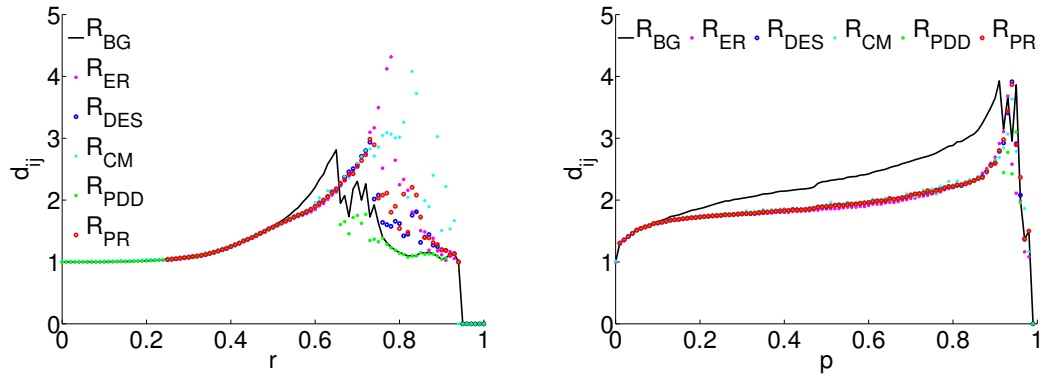


FIGURE B.2: Shortest pathway of the brain graphs and random graphs, FC map related graphs on the left and AC map related graphs on the right.

The R_{BG} network of FCM seems to be less segregated than the randomized networks while r lies between $[0.65, 0.95]$. This is the threshold value at which the R_{BG} network of FCM begins to get multiple components. The R_{BG} network of ACM tends to be more segregated than its random networks. Whenever all the nodes get sparse (approximately $r > 0.95, p > 0.98$) in both FCM and ACM networks, the shortest pathway is represented as 0.

B.3 Global Efficiency

The global efficiency E is measured as the average of the inverse shortest pathway,

$$E = \frac{1}{n} \sum_{i \in N} E_i = \frac{1}{n} \sum_{i \in N} \frac{\sum_{j \in N, j \neq i} d_{ij}^{-1}}{n - 1}, \quad (\text{B.3})$$

where E_i is the global efficiency of node, d_{ij} is the shortest pathway between nodes i and j [22]. As seen from the equation, global efficiency becomes larger with smaller shortest pathways between nodes. The global efficiency is a measure of the integration in the network. It reveals the strength of connections in a network. Global efficiency measures the ability of a network to transmit information at the global level [51].

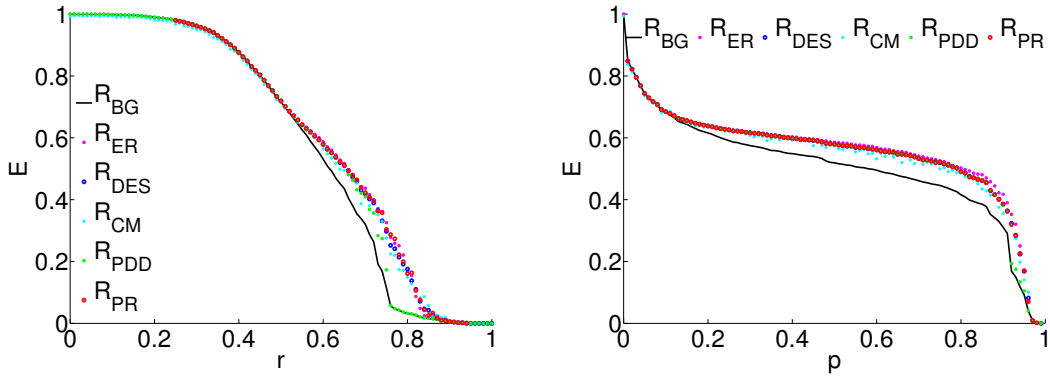


FIGURE B.3: Global efficiencies of the original networks and random graphs; FCM on left side, ACM on right side.

All randomly constructed graphs tend to have slightly higher E than that of brain graphs. If it is easier to visit a node starting from any other node in the graph, the information transmission capacity is expected to be more robust. When Figure B.2 and B.3 are compared, it can be inferred that higher d_{ij} values reveals lower global efficiency in a network.

B.4 Local Efficiency

The local efficiency E_{loc} is measured as the average of inverse shortest pathways between nodes in neighborhood of a specific node,

$$E_{loc} = \frac{1}{n} \sum_{i \in N} E_{loc,i} = \frac{1}{n} \sum_{i \in N} \frac{\sum_{j,h \in N, j \neq i} a_{ij} a_{ih} [d_{jh}(N_i)]^{-1}}{k_i(k_i - 1)} , \quad (\text{B.4})$$

where $E_{loc,i}$ is the local efficiency of node i , $d_{jh}(N_i)$ is the shortest pathway between nodes j and h , which are located in neighborhood of node i [22]. Local efficiency measures the ability of a network to transmit information at the local level [51].

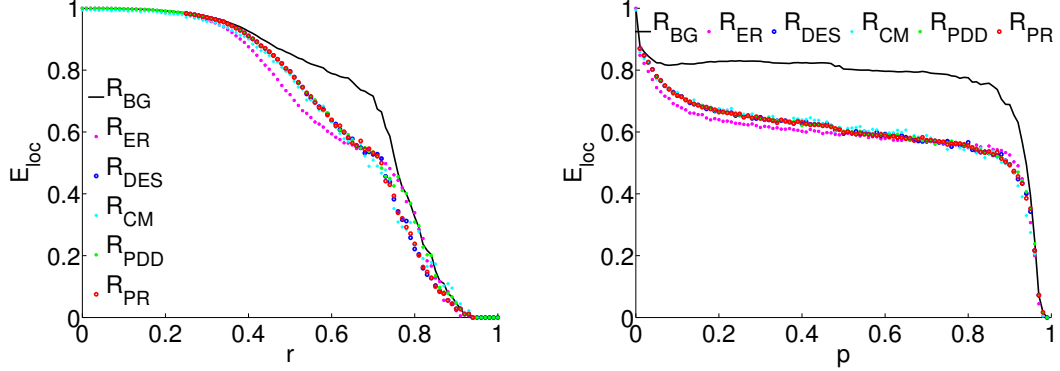


FIGURE B.4: E_{loc} of the functional connectivity map derived R_{BG} and its randomized networks on the left and E_{loc} of the anatomical map derived R_{BG} and its randomized networks on the right.

Brain graphs based on FCM and ACM tend to have higher E_{loc} than their random graphs. Anatomical connectivity matrix related networks have in general higher E_{loc} compared to the functional connectivity matrix related networks. Local information transmit is more efficient in ACM than in FCM. The graphs with larger E compared to the R_{BG} in Figure B.3 exhibit lower E_{loc} in Figure B.4.

B.5 Small Worldness

A small world network is both highly segregated and integrated, a measure of small worldness S was proposed to capture this effect in a single statistic,

$$S = \frac{C/C_{rand}}{L/L_{rand}} , \quad (\text{B.5})$$

where C and C_{rand} are clustering coefficients, L and L_{rand} are characteristic path lengths of the original and random network respectively [25]. The random network here is

constructed with *Erdős-Rényi* method, which has the same number of nodes and links as the reference graph:

$$L = \frac{1}{n} \sum_{i \in N} L_i = \frac{1}{n} \sum_{i \in N} \frac{\sum_{j \in N, j \neq i} d_{ij}}{n - 1}. \quad (\text{B.6})$$

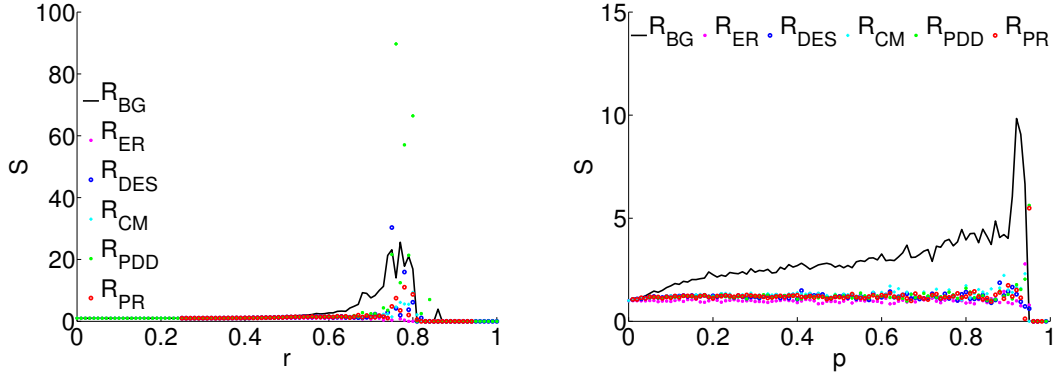


FIGURE B.5: Small worldness of the anatomical (left) and functional (right) brain graphs and their random graphs.

In Figure B.5, brain graphs have higher S than random graphs for both FCM and ACM. In comparison to other network measurements up to here, S measure makes brain graphs the most distinguishable than random graphs. At some unique r and p values, random graphs R_{DES} , R_{PDD} (left) and R_{PDD} , R_{PR} (right) tend to have quite large S . However, this does not change the general high S pattern of brain graphs. Random networks seem to be equally segregated and integrated in general, but the real networks behave differently.

B.6 Assortativity

Assortativity measures the correlation coefficient between the degrees of all nodes on two opposite ends of a link [20]. Assortativity coefficient A of a network is given by the following equation;

$$A = \frac{\frac{1}{l} \sum_{(i,j) \in L} k_i k_j - \left(\frac{1}{2L} \sum_{(i,j) \in L} k_i + k_j \right)^2}{\frac{1}{2L} \sum_{(i,j) \in L} (k_i^2 + k_j^2) - \left(\frac{1}{2L} \sum_{(i,j) \in L} k_i + k_j \right)^2}, \quad (\text{B.7})$$

where L is number of edges in, k_i is degree of node i [52].

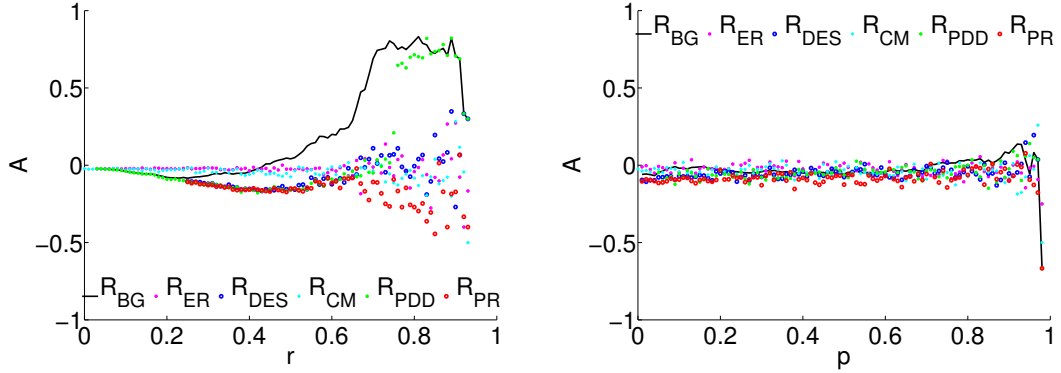


FIGURE B.6: Assortativity coefficients of FCM (left) and ACM (right) brain graphs and their random graphs.

Negative assortativity presents a network having widely distributed high-degree hubs [20]. On the other hand, assortativity coefficients close to 1 indicates a graph having fine correlated degree nodes. A -values follow a very similar pattern around 0 for all the graphs based on ACM as seen in Figure B.6. The degrees of nodes seem not to be significantly correlated. However, A -values of FCM related networks are more diverse. The degrees of nodes are highly correlated in FCM brain graph, particularly at large r , whereas random graphs exhibit anti-correlations among node degrees.

B.7 Average Connected Components

The connected components of an indirected graph indicates the number of subgraphs in overall network. Subgraph can be imagined as a connected group of nodes which have globally no connection to any other subgraph. In order to visualize subgraphs algebraically, let us define number of edges L of graph G in terms of three subgraphs of G :

$$L_G = L_{G_1} \cup L_{G_2} \cup L_{G_3}. \quad (\text{B.8})$$

We can expect that the nodes are assumed to be well connected at lower r and p , it is always possible to reach any node in the network starting from any other node. That means subgraphs should begin to be constructed after a high r and p values. Average connected components ACC measure is calculated via NETWORKX tool for all graphs in this project [30].

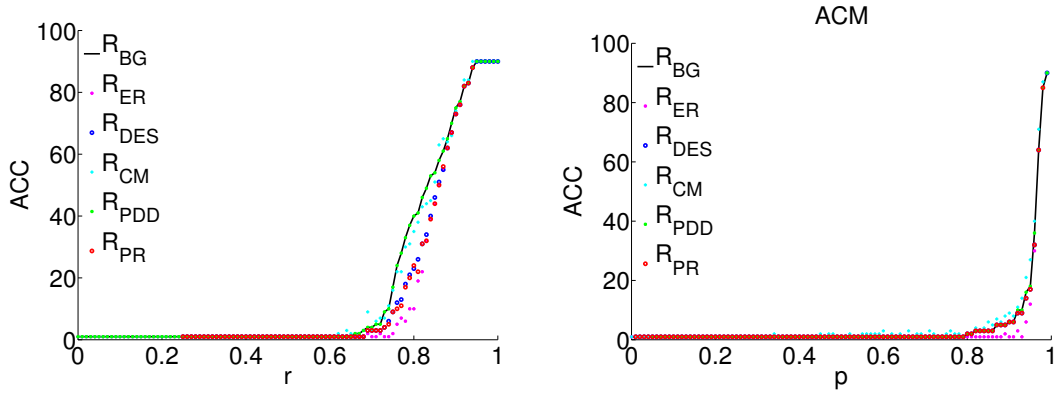


FIGURE B.7: Assortativity coefficients of FCM (left) and ACM (right) brain graphs and their random graphs.

Figure B.7 shows that, at higher r and p levels, the nodes become sparse as the network densities get lower in FCM and ACM graphs. When $r > 0.95$ and $p = 1.00$, we can imagine each node as a single subgraph, since none of the nodes is connected and therefore ACC becomes equals to 90, which is exactly the total number of nodes in all graph types.

B.8 Degree Distribution

Degree distribution of a network $p(k)$ reflects the probability of a node to have a given number of degree k . Figures B.8 and B.9 illustrates $p(k)$ for functional connectivity map (FCM) and anatomical connectivity map (ACM) related brain graphs and their randomized networks. It can be seen that, at lower threshold r - or probability p -values (here, p is used to generate the adjacency matrix), the networks tend to be highly dense by means of number of edges in graph (see Section 2.4.1 and Figure B.1). For instance, at $r = 0$, the probability of any node to have 89 edges $p(k = 89)$ is equal to 1.0, each node is connected to all other nodes. At high r -values, $p(k = 0)$ dominates.

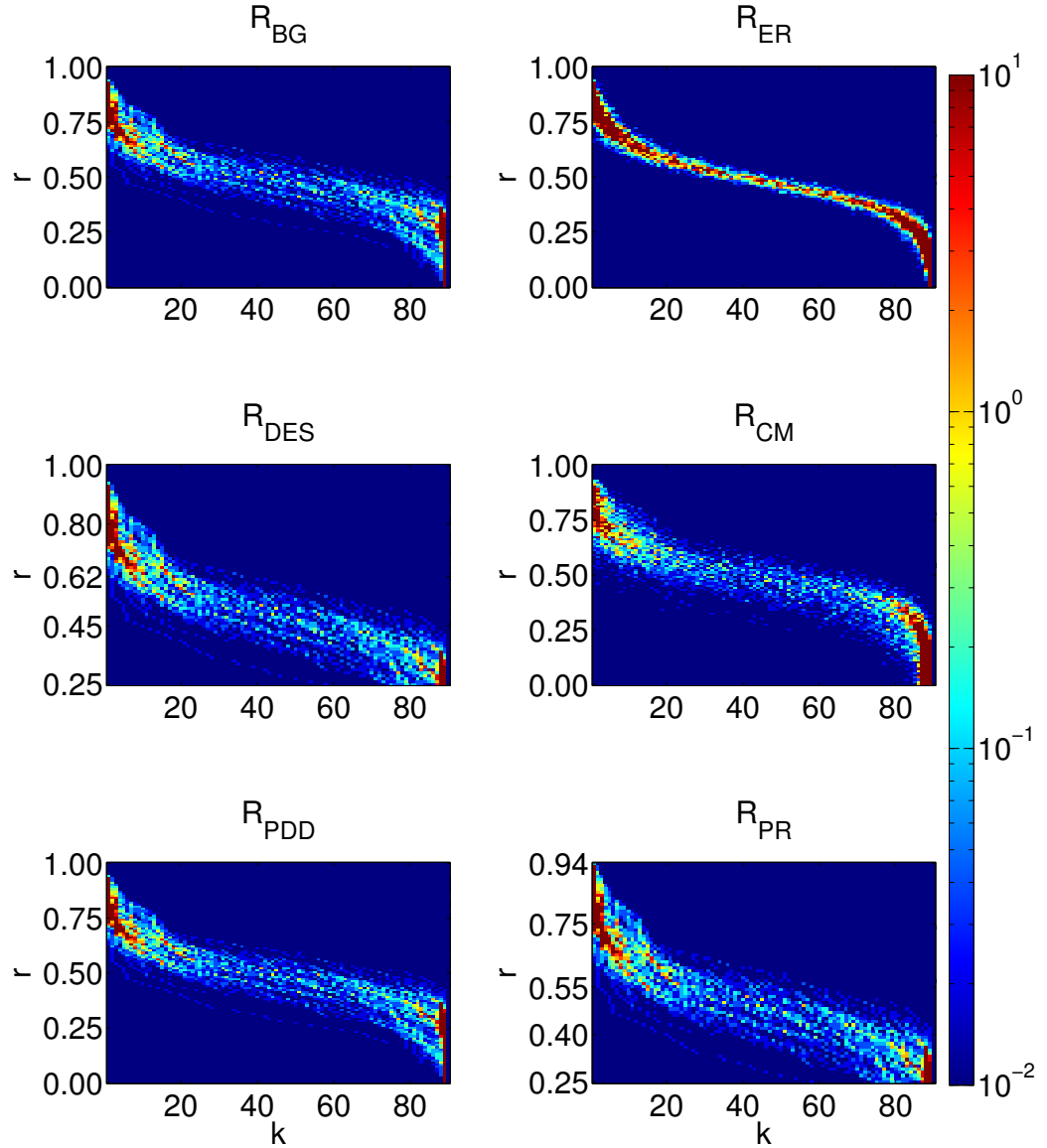


FIGURE B.8: Heat maps of $p(k)$ of the brain graph R_{BG} constructed on the functional connectivity map obtained from fMRI-BOLD measurement and its randomly generated networks. The limits of colorbar are in logarithmic scale.

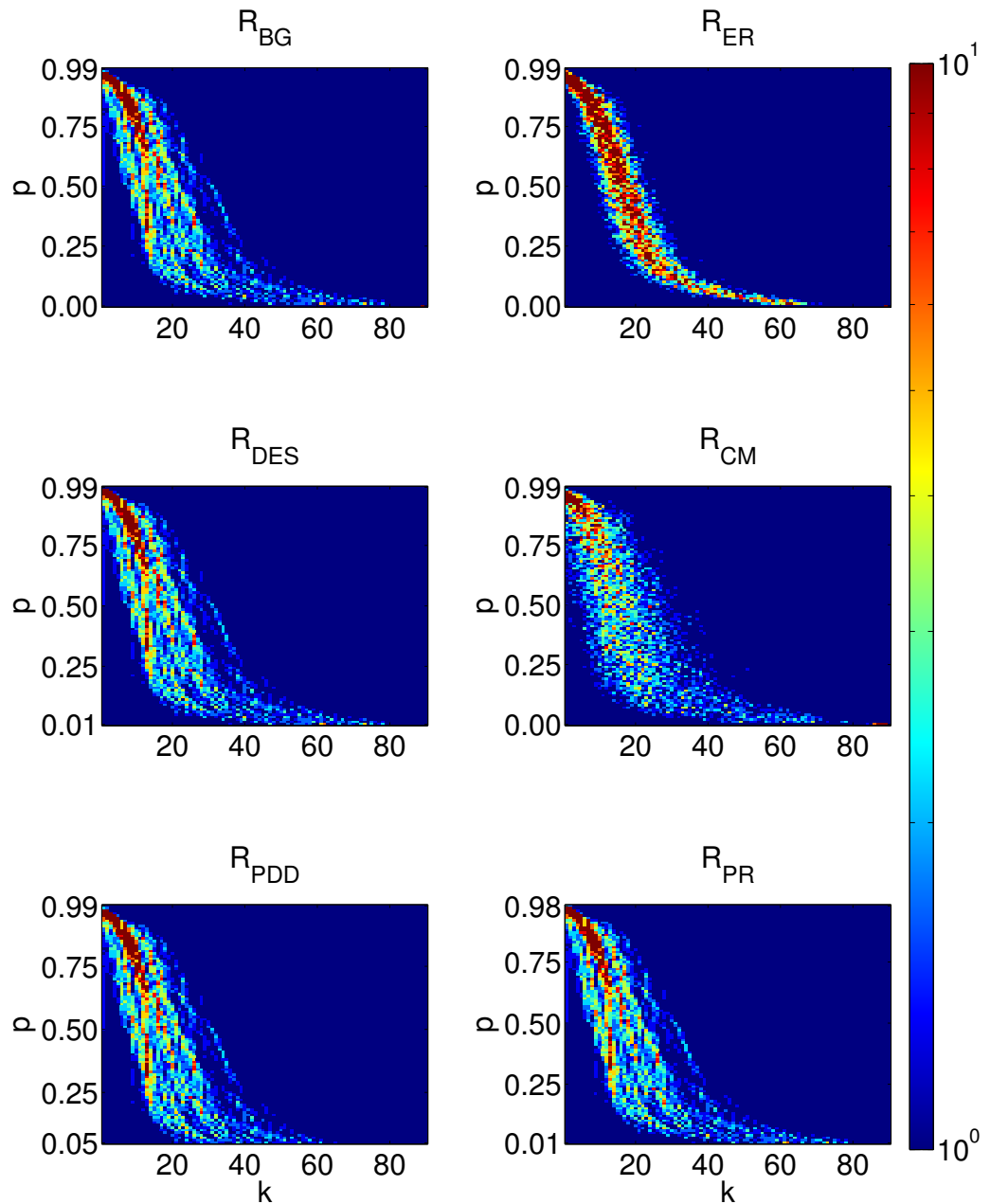


FIGURE B.9: Heat maps of $p(k)$ of the brain graph R_{BG} constructed on the anatomical connectivity map obtained from DW-MRI measurement and its randomly generated networks. The limits of colorbar are in logarithmic scale.

B.9 Clustering Coefficient of Nodes

The clustering coefficient of each node C_i is measured as ratio between number of triangles around a node and all possible edge connections of that node $\binom{k_i}{2}$ [23],

$$C_i = \frac{2t_i}{k_i(k_i - 1)} . \quad (\text{B.9})$$

As the number of triangles around a node increased, C_i becomes larger indicating more segregated nodes in the network.

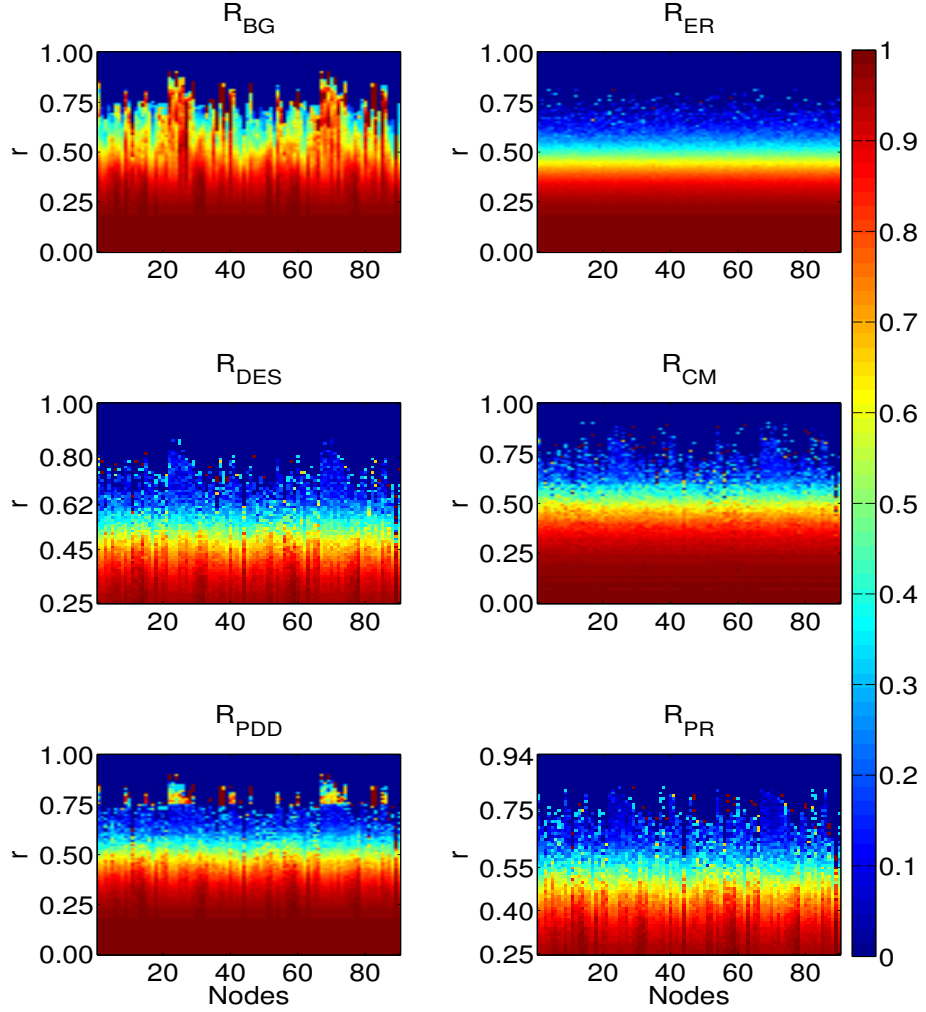


FIGURE B.10: Heat maps of C_i of the brain graph R_{BG} , which is constructed on the functional connectivity map obtained from fMRI-BOLD measurement, and its randomly generated networks.

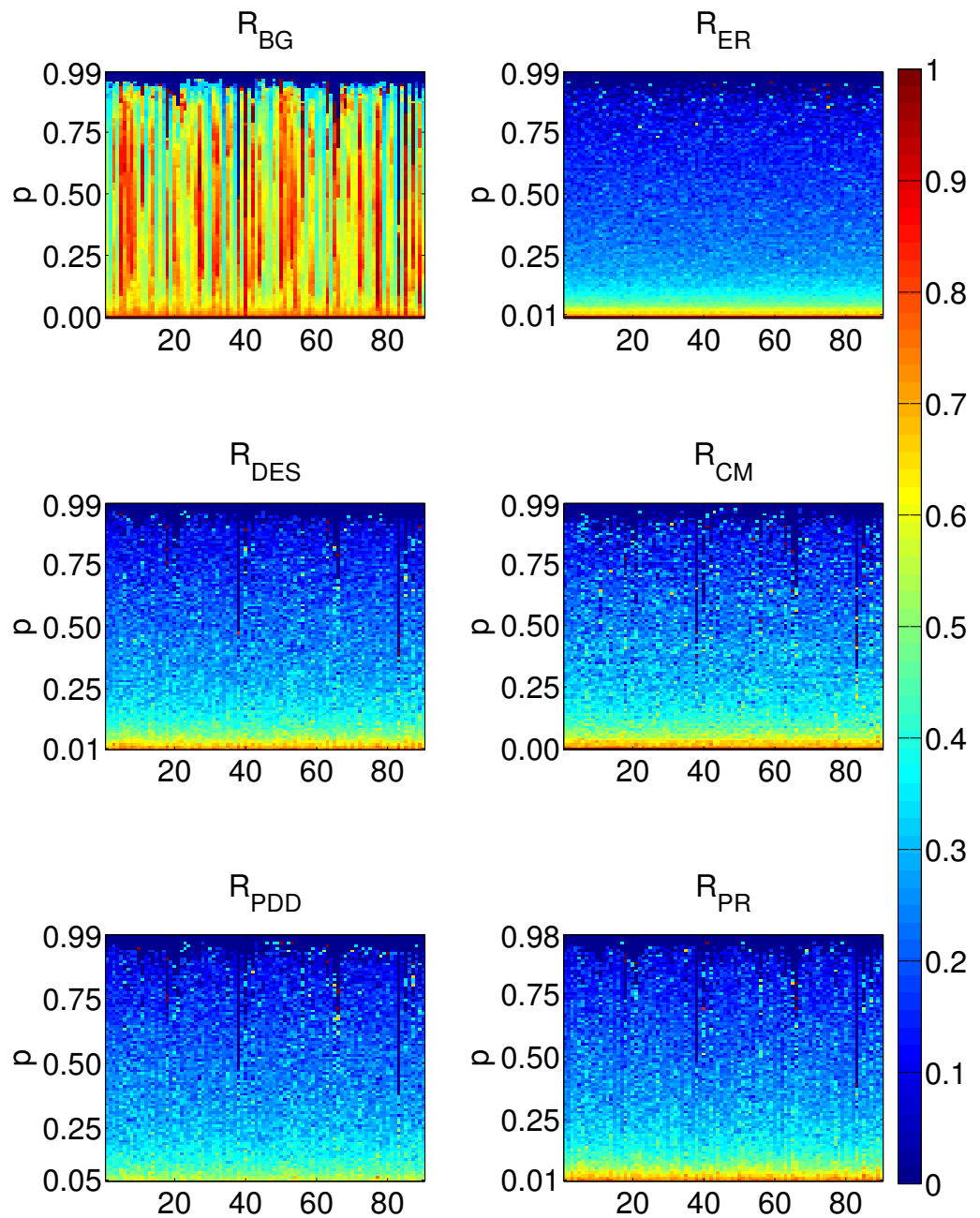


FIGURE B.11: Heat maps of C_i of the brain graph R_{BG} , which is constructed on the anatomical connectivity map obtained from DW-MRI measurement, and its randomly generated networks.

Appendix C

Empirical Distance Matrices

The distance matrix d_{ij} is one of the ingredient parameters of the FHN network model. It is used to quantify the time delays Δt_{ij} between nodes i and j , i.e. $\Delta t_{ij} = d_{ij}/v$, where v is the signal propagation velocity along the axons [5, 11]. The neuronal time-series of functionally and anatomically derived adjacency matrices is extracted by using different d_{ij} data. For the FCM, d_{ij} is the matrix of Euclidean distances between centers of brain regions from which BOLD time series are extracted [39]. For the ACM, d_{ij} is empirically provided with together with anatomical connectivity map [28].

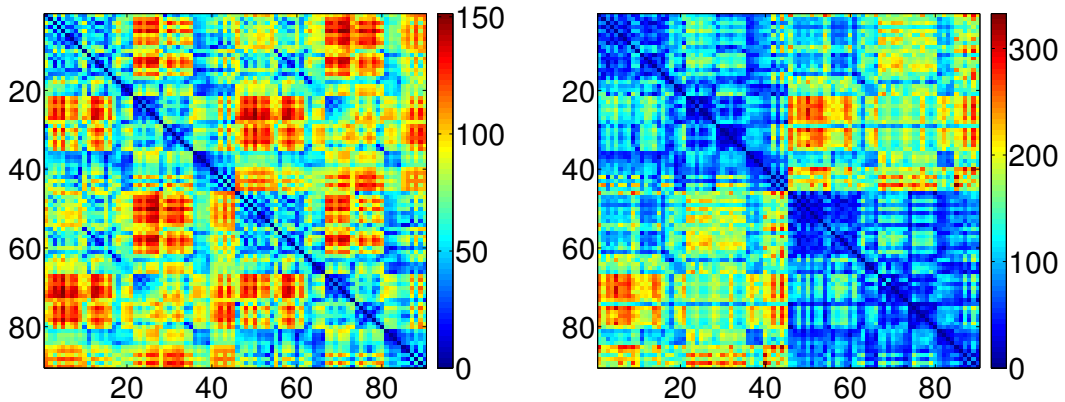


FIGURE C.1: d_{ij} of the functional connectivity map (left) and anatomical connectivity map (right). The colorbars are in units of mm.

Bibliography

- [1] B. Biswal, F. Z. Yetkin, V. M. Haughton, and J. S. Hyde. Functional connectivity in the motor cortex of resting human brain using echo-planar MRI. *Magnetic Resonance in Medicine*, 34(4):537–541, 1995.
- [2] J. S. Damoiseaux, S. A. R. B. Rombouts, F. Barkhof, P. Scheltens, C. J. Stam, S. M. Smith, and C. F. Beckmann. Consistent resting-state networks across healthy subjects. *Proc. Natl. Acad. Sci. U.S.A.*, 103(37):13848–13853, 2006.
- [3] S. L. Bressler and V. Menon. Large-scale brain networks in cognition: emerging methods and principles. *Trends in Cognitive Sciences*, 14(6):277–290, 2010.
- [4] N. Tzourio-Mazoyer, B. Landeau, D. Papathanassiou, F. Crivello, O. Etard, N. Delcroix, B. Mazoyer, and M. Joliot. Automated anatomical labeling of activations in SPM using a macroscopic anatomical parcellation of the MNI MRI single-subject brain. *Neuroimage*, 15(1):273–289, 2002.
- [5] V. Vuksanović and P. Hövel. Large-scale neural network model for functional networks of the human cortex. In A. Pelster and G Wunner, editors, *Selforganization in Complex Systems: The Past, Present, and Future of Synergetics, Proc. of the International Symposium, Hanse Institute of Advanced Studies Delmenhorst*, Berlin, 2014. Springer.
- [6] K. Friston, A. Mechelli, R. Turner, and C. J. Price. Nonlinear responses in fMRI: The balloon model, Volterra kernels, and other hemodynamics. *NeuroImage*, 12(4):466–477, 2000.
- [7] V. Vuksanović and P. Hövel. Functional connectivity of distant cortical regions: Role of remote synchronization and symmetry in interactions. *NeuroImage*, 97:1–8, 2014.

- [8] M. Rubinov, O. Sporns, C. van Leeuwen, and M. Breakspear. Symbiotic relationship between brain structure and dynamics. *BMC Neuroscience*, 10(1):55, 2009.
- [9] C. J. Honey, R. Kötter, M. Breakspear, and O. Sporns. Network structure of cerebral cortex shapes functional connectivity on multiple time scales. *Proc. Natl. Acad. Sci. U.S.A.*, 104:10240–10245, 2007.
- [10] A. Ghosh, Y. Rho, A. R. McIntosh, R. Kötter, and V. K. Jirsa. Noise during rest enables the exploration of the brain’s dynamic repertoire. *PLoS Comput Biol*, 4 (10):e1000196, 2008.
- [11] A. Ghosh, Y. Rho, A. R. McIntosh, R. Kötter, and V. K. Jirsa. Cortical network dynamics with time delays reveals functional connectivity in the resting brain. *Cogn. Neurodyn.*, 2(2):115–120, 2008.
- [12] G. Deco, V. K. Jirsa, A. R. McIntosh, O. Sporns, and R. Kötter. Key role of coupling, delay, and noise in resting brain fluctuations. *Proc. Natl. Acad. Sci. U.S.A.*, 106(25):10302–10307, 2009.
- [13] J. Cabral, E. Hugues, O. Sporns, and G. Deco. Role of local network oscillations in resting-state functional connectivity. *NeuroImage*, 57(1):130–139, 2011.
- [14] J. Cabral, E. Hugues, M. L. Kringselbach, and G. Deco. Modeling the outcome of structural disconnection on resting-state functional connectivity. *NeuroImage*, 62: 1342–1353, 2012.
- [15] E. T. Bullmore and O. Sporns. Complex brain networks: graph theoretical analysis of structural and functional systems. *Nat. Rev. Neurosci.*, 10(3):186–198, 2009.
- [16] C. J. Stam. Characterization of anatomical and functional connectivity in the brain: A complex networks perspective. *Int. J. Psychophysiol.*, 77(3):186–194, 2010. PROCEEDINGS OF THE 15TH WORLD CONGRESS OF PSYCHOPHYSIOLOGY of the International Organization of Psychophysiology (I.O.P.) Budapest, Hungary September 1-4, 2010.
- [17] M. E. J. Newman. *Networks: an introduction*. Oxford University Press, Inc., New York, 2010.
- [18] M. Rubinov and O. Sporns. Weight-conserving characterization of complex functional brain networks. *NeuroImage*, 56(4):2068–2079, 2011.

- [19] A. L. Barabási. Scale-free networks: a decade and beyond. *Science*, 325(5939):412–413, 2009.
- [20] M. Rubinov and O. Sporns. Complex network measures of brain connectivity: uses and interpretations. *NeuroImage*, 52(3):1059–1069, 2010.
- [21] K. J. Friston. Functional and effective connectivity in neuroimaging: a synthesis. *Human brain mapping*, 2(1-2):56–78, 1994.
- [22] V. Latora and M. Marchiori. Efficient behavior of small-world networks. *Phys. Rev. Lett.*, 87(19):198701, 2001.
- [23] D. J. Watts and S. H. Strogatz. Collective dynamics of ‘small-world’ networks. *Nature*, 393:440–442, 1998.
- [24] M. E. J. Newman. The structure and function of complex networks. *SIAM Review*, 45(2):167–256, 2003.
- [25] M. D. Humphries and K. Gurney. Network ‘small-world-ness’ : a quantitative method for determining canonical network equivalence. *PLoS One*, 3(4):e0002051, 2008.
- [26] M. P. van den Heuvel and O. Sporns. Rich-club organization of the human connectome. *The Journal of Neuroscience*, 31(44):15775–15786, 2011.
- [27] E. T. Bullmore and D. S. Bassett. Brain graphs: graphical models of the human brain connectome. *Annual review of clinical psychology*, 7:113–140, 2011.
- [28] Y. Iturria-Medina, R. C. Sotero, E. J. Canales-Rodríguez, Y. Alemán-Gómez, and L. Melie-García. Studying the human brain anatomical network via diffusion-weighted MRI and graph theory. *Neuroimage*, 40(3):1064–1076, 2008.
- [29] M. Xia, J. Wang, and Y. He. Brainnet viewer: a network visualization tool for human brain connectomics. *PLoS One*, 8(7):e68910, 2013.
- [30] A. A. Hagberg, D. A. Schult, and P. J. Swart. Exploring network structure, dynamics, and function using NetworkX. *Proceedings of the 7th Python in Science Conference (SciPy2008)*, pages 11–15, August 2008.
- [31] P. Erdős and A. Rényi. On random graphs. i. *Publicationes Mathematicae*, 6:290–297, 1959.

- [32] A. L. Barabási and R. Albert. Emergence of scaling in random networks. *Science*, 286:509, 1999.
- [33] M. Rubinov and O. Sporns. Complex network measures of brain connectivity: uses and interpretations. *Neuroimage*, 52(3):1059–1069, 2010.
- [34] R. L. Buckner, J. Sepulcre, T. Talukdar, F. M. Krienen, H. Liu, T. Hedden, J. R. Andrews-Hanna, R. A. Sperling, and K. A. Johnson. Cortical hubs revealed by intrinsic functional connectivity: mapping, assessment of stability, and relation to alzheimer’s disease. *The Journal of Neuroscience*, 29(6):1860–1873, 2009.
- [35] J. S. Damoiseaux and M. D. Greicius. Greater than the sum of its parts: a review of studies combining structural connectivity and resting-state functional connectivity. *Brain Structure and Function*, 213(6):525–533, 2009.
- [36] J. L. Vincent, G. H. Patel, M. D. Fox, A. Z. Snyder, J. T. Baker, D. C. van Essen, J. M. Zempel, L. H. Snyder, M. Corbetta, and M. E. Raichle. Intrinsic functional architecture in the anaesthetized monkey brain. *Nature*, 447(7140):83–86, 2007.
- [37] R. FitzHugh. Impulses and physiological states in theoretical models of nerve membrane. *Biophys. J.*, 1:445–466, 1961.
- [38] J. Nagumo, S. Arimoto, and S. Yoshizawa. An active pulse transmission line simulating nerve axon. *Proc. IRE*, 50:2061–2070, 1962.
- [39] M. Kaiser and C. C. Hilgetag. Nonoptimal component placement, but short processing paths, due to long-distance projections in neural systems. *PLoS Comput. Biol.*, 2(7):e95, 2006.
- [40] V. Flunkert and E. Schöll. pydelay – a python tool for solving delay differential equations. arXiv:0911.1633 [nlin.CD], 2009.
- [41] P. Bogacki and L. F. Shampine. A 3(2) pair of runge - kutta formulas. *Applied Mathematics Letters*, 2(4):321–325, 1989.
- [42] R. B. Buxton, E. C. Wong, and L. R. Frank. Dynamics of blood flow and oxygenation changes during brain activation: the balloon model. *Magnetic resonance in medicine*, 39(6):855–864, 1998.

- [43] N. P. Blockley, V. E. M. Griffeth, A. B. Simon, and R. B. Buxton. A review of calibrated blood oxygenation level-dependent (BOLD) methods for the measurement of task-induced changes in brain oxygen metabolism. *NMR in Biomedicine*, 26(8):987–1003, 2013.
- [44] A. K. Seth, P. Chorley, and L. C. Barnett. Granger causality analysis of fMRI BOLD signals is invariant to hemodynamic convolution but not downsampling. *Neuroimage*, 65:540–555, 2013.
- [45] K. Irikura, K. I. Maynard, and M. A. Moskowitz. Importance of nitric oxide synthase inhibition to the attenuated vascular responses induced by topical l-nitroarginine during vibrissal stimulation. *Journal of Cerebral Blood Flow & Metabolism*, 14(1):45–48, 1994.
- [46] J. Mayhew, D. Hu, Y. Zheng, S. Askew, Y. Hou, J. Berwick, P. J. Coffey, and N. Brown. An evaluation of linear model analysis techniques for processing images of microcirculation activity. *Neuroimage*, 7(1):49–71, 1998.
- [47] K. L. Miller, W. M. Luh, T. T. Liu, A. Martinez, T. Obata, E. C. Wong, L. R. Frank, and R. B. Buxton. Characterizing the dynamic perfusion response to stimuli of short duration. In *Proc. ISRM*, volume 8, page 580, 2000.
- [48] K. J. Friston, O. Josephs, G. Rees, and R. Turner. Nonlinear event-related responses in fMRI. *Magnetic resonance in medicine*, 39(1):41–52, 1998.
- [49] J. B. Mandeville, J. J. A. Marota, C. Ayata, G. Zaharchuk, M. A. Moskowitz, B. R. Rosen, and R. M. Weisskoff. Evidence of a cerebrovascular postarteriole windkessel with delayed compliance. *Journal of Cerebral Blood Flow & Metabolism*, 19(6):679–689, 1999.
- [50] A. Bhattacharyya. On a measure of divergence between two statistical populations defined by their probability distributions. *Bulletin of the Calcutta Mathematical Society*, 35:99–109, 1943.
- [51] D. S. Bassett and E. T. Bullmore. Human brain networks in health and disease. *Current opinion in neurology*, 22(4):340, 2009.
- [52] M. E. J. Newman. Assortative mixing in networks. *Phys. Rev. Lett.*, 89:208701, 2002.